

A hybrid topological quantum state in an elemental solid




<https://doi.org/10.1038/s41586-024-07203-8>

Received: 22 February 2023

Accepted: 16 February 2024

Published online: 10 April 2024

 Check for updates

Md Shafayat Hossain^{1,11}, Frank Schindler^{2,11}, Rajibul Islam^{3,4,11}, Zahir Muhammad^{5,11}, Yu-Xiao Jiang^{1,11}, Zi-Jia Cheng^{1,11}, Qi Zhang¹, Tao Hou⁶, Hongyu Chen⁶, Maksim Litskevich¹, Brian Casas⁷, Jia-Xin Yin¹, Tyler A. Cochran¹, Mohammad Yahyavi⁶, Xian P. Yang¹, Luis Balicas⁷, Guoqing Chang⁶, Weisheng Zhao⁵, Titus Neupert⁸ & M. Zahid Hasan^{1,9,10}

Topology^{1–3} and interactions are foundational concepts in the modern understanding of quantum matter. Their nexus yields three important research directions: (1) the competition between distinct interactions, as in several intertwined phases, (2) the interplay between interactions and topology that drives the phenomena in twisted layered materials and topological magnets, and (3) the coalescence of several topological orders to generate distinct novel phases. The first two examples have grown into major areas of research, although the last example remains mostly unexplored, mainly because of the lack of a material platform for experimental studies. Here, using tunnelling microscopy, photoemission spectroscopy and a theoretical analysis, we unveil a ‘hybrid’ topological phase of matter in the simple elemental-solid arsenic. Through a unique bulk-surface-edge correspondence, we uncover that arsenic features a conjoined strong and higher-order topology that stabilizes a hybrid topological phase. Although momentum-space spectroscopy measurements show signs of topological surface states, real-space microscopy measurements unravel a unique geometry of topologically induced step-edge conduction channels revealed on various natural nanostructures on the surface. Using theoretical models, we show that the existence of gapless step-edge states in arsenic relies on the simultaneous presence of both a non-trivial strong Z_2 invariant and a non-trivial higher-order topological invariant, which provide experimental evidence for hybrid topology. Our study highlights pathways for exploring the interplay of different band topologies and harnessing the associated topological conduction channels in engineered quantum or nano-devices.

Despite its dubious reputation as the ‘king of poisons’, arsenic (As) has long been used in semiconductor technology, tonics and even for cancer treatment⁴. Here we find that the most stable form of As, namely α -As⁵, hosts a novel quantum phase of matter, which, at low energies, can be understood with the mathematical framework of topology^{1–3}. Prototypical examples of this class of materials are topological insulators, which act as an insulator in their interior but feature time-reversal-symmetry-protected conducting states on the surface or edge^{1–3,6–8}. In particular, strong (or first-order) topological insulators in three-dimensional crystals are gapped in the bulk but stabilize gapless surface states, whereas higher-order topological insulators are also gapped on their surfaces but host one-dimensional gapless hinge modes^{9–12}. The controllability of such topologically protected conduction channels has garnered immense interest in energy-saving

technology and quantum information science. By combining first- and higher-order topology in a single material, this work provides a route to the precise control of a single-crystal quantum system. Leveraging a combination of experiments and theory, we find that α -As carries simultaneous topological modes on the surface and along the step edge(s). Notably, we show that the step-edge modes appear only for selected, crystalline-symmetry-allowed orientations, which, unlike surface or hinge states, are not expected for either first- or higher-order topological insulators but only for a hybrid material in which both kinds of band topology are present.

The discussion of the electronic structure of α -As is facilitated by the presence of inversion symmetry, which allows us to designate the bands at high-symmetry momenta with inversion eigenvalues. The number of plus and minus eigenvalues below the Fermi level reveals the so-called

¹Laboratory for Topological Quantum Matter and Advanced Spectroscopy (B7), Department of Physics, Princeton University, Princeton, NJ, USA. ²Blackett Laboratory, Imperial College London, London, UK. ³International Research Centre MagTop, Institute of Physics, Polish Academy of Sciences, Warsaw, Poland. ⁴Department of Physics, University of Alabama at Birmingham, Birmingham, AL, USA. ⁵Hefei Innovation Research Institute, School of Integrated Circuit Science and Engineering, Beihang University, Hefei, P.R. China. ⁶Division of Physics and Applied Physics, School of Physical and Mathematical Sciences, Nanyang Technological University, Singapore, Singapore. ⁷National High Magnetic Field Laboratory, and Physics Department, Florida State University, Tallahassee, FL, USA. ⁸Department of Physics, University of Zurich, Zurich, Switzerland. ⁹Princeton Institute for Science and Technology of Materials, Princeton University, Princeton, NJ, USA. ¹⁰Quantum Science Center (QSC, ORNL), Oak Ridge, TN, USA. ¹¹These authors contributed equally: Md Shafayat Hossain, Frank Schindler, Rajibul Islam, Zahir Muhammad, Yu-Xiao Jiang, Zi-Jia Cheng. ✉e-mail: mdsh@princeton.edu; f.schindler@imperial.ac.uk; mzh Hasan@princeton.edu

band inversions in momentum space and links to symmetry-indicator topological invariants^{13–15}. α -As features a series of band inversions around the Fermi level that combine to produce its hybrid topology^{16–19}: (1) A double band inversion at the Γ point of the rhombohedral (primitive) Brillouin zone, which, on its own, would result in a higher-order topological insulator with gapped surfaces but helical hinge states¹⁴. (2) A single band inversion at the three C_3 -related L points of the rhombohedral Brillouin zone (Extended Data Fig. 1a), which is expected to lead to a first-order topological insulator¹³ with gapless Dirac-cone surface states. Existing angle-resolved photoemission spectroscopy (ARPES) work on α -As has explored the first-order topological insulator state¹⁶, reporting topological Rashba-type, spin-split surface states. However, a real-space investigation into how the higher-order topology is intertwined with the first-order topological insulator phase remains lacking. Owing to its high spatial resolution, electronic detection and magnetic field tunability, scanning tunnelling microscopy (STM) can visualize the topological boundary modes directly in real space^{20–34}. By revealing gapless step-edge-localized states, our STM measurements expose the unique, hybrid, first- and higher-order topology of α -As.

Observation of surface state

We start with the surface characterization of α -As. The crystalline lattice has a rhombohedral primitive cell with a space group of $R\bar{3}m$ (No. 166). In the following, we work with the hexagonal (conventional) cell for convenience. As illustrated in Fig. 1a, the crystal can be regarded as a stack of As bilayers along the c axis. The As atoms within the bilayer form a buckled honeycomb lattice, and cleaving leaves a triangular lattice in the ab plane (Fig. 1b). Using STM on a freshly cleaved sample, we visualized the large surface area shown in Fig. 1c, which has an atomically resolved triangular lattice (Fig. 1c top inset) with sharp Bragg peaks in the Fourier transform image (Fig. 1c bottom inset). Figure 1d summarizes our energy-resolved tunnelling spectroscopy measurements on a clean region taken over a large distance. The averaged spectrum reveals a soft gap, namely, a suppression in the spectral weight near the Fermi energy. Figure 1e shows the temperature-dependent resistance data measured in a bulk α -As sample while passing a current along the ab plane. Here, the resistance decreases as the sample is cooled down, indicative of a metallic state on the surface. Indeed, the presence of such a surface state is captured by our ARPES measurements. Figure 1f, where we plot the second derivative of an energy–momentum cut along the $\bar{\Gamma} \rightarrow \bar{M}$ direction of the surface Brillouin zone (Extended Data Fig. 1a), provides such data. We observe a pair of sharp, parabolic, surface bands that is consistent with both previous photoemission work¹⁶ and our first-principles calculations (Fig. 1g), indicating the presence of a topological Rashba-like surface state (see also Extended Data Figs. 1 and 2) along $\bar{\Gamma} \rightarrow \bar{M}$. Note that, when projected on the surface Brillouin zone, the bulk spectrum is gapped along the $\bar{\Gamma} \rightarrow \bar{M}$ line (Extended Data Fig. 1). Hence, the surface state within the bulk gap marks the topological bulk boundary correspondence and indicates a first-order topological insulator phase in α -As. Additional photoemission spectroscopy and first-principles calculation results pertaining to the topological surface state in α -As are summarized in Extended Data Figs. 1 and 2.

Notably, the surface state also manifests in our real-space imaging. Our approach invokes the quasiparticle interference in the ab plane. Extended Data Fig. 3, which captures the results of such experiments, shows a prominent scattering branch whose origin and shape match the parabolic surface band visualized in our photoemission spectroscopy (Fig. 1f) and first-principles calculations (Fig. 1g); see Supplementary Table 1 for a quantitative comparison between the three sets of data. Thus, quasiparticle interference spectroscopy provides a real-space detection of the presence of a surface state in α -As.

To gain insight into the surface state more quantitatively, we investigated the Landau quantization in α -As using tunnelling spectroscopy

measurements under perpendicular magnetic fields and constructed a Landau fan diagram^{33,35–38}. As a function of energy and magnetic field, the tunnelling spectra form the Landau fan diagram shown in Fig. 1h (see Extended Data Fig. 4 for details). A close examination of Fig. 1h reveals two sets of electron-type Landau fans, which can be fitted to the Rashba-split up- and down-spin Landau levels (marked with colour-coded dashed lines in Fig. 1h) stemming from the Rashba-split surface state in α -As. Here, the terms ‘spin up’ and ‘spin down’ refer to two sets of electronic structures with opposite spin directions, without specifying any particular direction (see ‘Mapping the Landau fan diagram’ in Methods for details).

Observation of step-edge state

Next, we investigated the electronic structure of its step edges. We derived dI/dV spectroscopic maps at a monolayer step edge along the a -axis direction identified by a topographic image (Fig. 2a). We found that the step edge exhibits pronounced step-edge states within the soft gap (spectroscopic images in Fig. 2a). Figure 2b captures the line profile obtained from the dI/dV map, demonstrating an exponential decay (with a characteristic length of $r_0 \approx 2.1$ nm) of the step-edge state on the crystal side. The step-edge state decayed more sharply on the vacuum side. The corresponding topographic line cut is presented in Fig. 2c. Further spectroscopic measurements taken perpendicular to the step edge (Fig. 2d) revealed a peak in the step-edge spectra (orange curves) near the Fermi energy (at approximately -5 mV) where the spectra away from the step edge (violet curves) exhibited a soft gap.

A topological edge state is protected by time-reversal symmetry, which can be broken by applying an external magnetic field. When we applied a magnetic field perpendicular to the ab plane, we found that the differential conductance measured at the step edge was suppressed substantially. The field-induced suppression of the step-edge state can be clearly seen in the dI/dV map taken at $B = 2$ T and shown in Fig. 2e. Upon further examination of the field-dependent tunnelling spectra (Fig. 2f for $B = 1, 2$ and 4 T), we found that an energy gap gradually developed at the step-edge state. The response of the step-edge state to an out-of-plane magnetic field is consistent with the established phenomenon in time-reversal symmetric materials, whereby the field induces the mixing of helical edge states and the opening of a Zeeman gap^{39–43}.

To investigate the quasiparticle interference of the step-edge state and compare it to that of the surface state, we used energy- and spatially resolved dI/dV spectroscopy perpendicular (top panel of Fig. 2g) and along (top panel of Fig. 2h) a monolayer step edge. In both cases, we observed pronounced ripple-like quantum interference patterns. By taking a one-dimensional Fourier transformation of the spectroscopic data with respect to the spatial location, we obtained quasiparticle scattering patterns perpendicular (bottom panel of Fig. 2g) and along (bottom panel of Fig. 2h) the step edge. The quasiparticle interference perpendicular to the step edge captured the parabolic dispersion of the surface state centred at $q = 0$, which is akin to the data shown in Extended Data Fig. 3c. In contrast, the quasiparticle spectrum along the step edge exhibited a single, sharp, scattering branch covering a distinct energy–momentum space, which is different from the scattering branch of the surface state shown in the bottom panel of Fig. 2g. Remarkably, this branch comes to an abrupt halt at finite momentum transfer with a distinct finite slope, a feature that cannot arise solely from a one-dimensional band dispersion. Instead, it aligns well with a band structure in which a step-edge band hybridizes with surface states at a finite momentum. A comparison between the edge quasiparticle interference (bottom panel of Fig. 2h) and the edge dI/dV spectra (Fig. 2f) reveals that the energy location of the dI/dV peak in the latter seems to coincide with the point of the dispersive branch vanishing in the former. Additional insights derived from a straightforward two-dimensional, lattice-based model are discussed in Supplementary Information section III. Notably, this contrasts with bismuth²³, for which

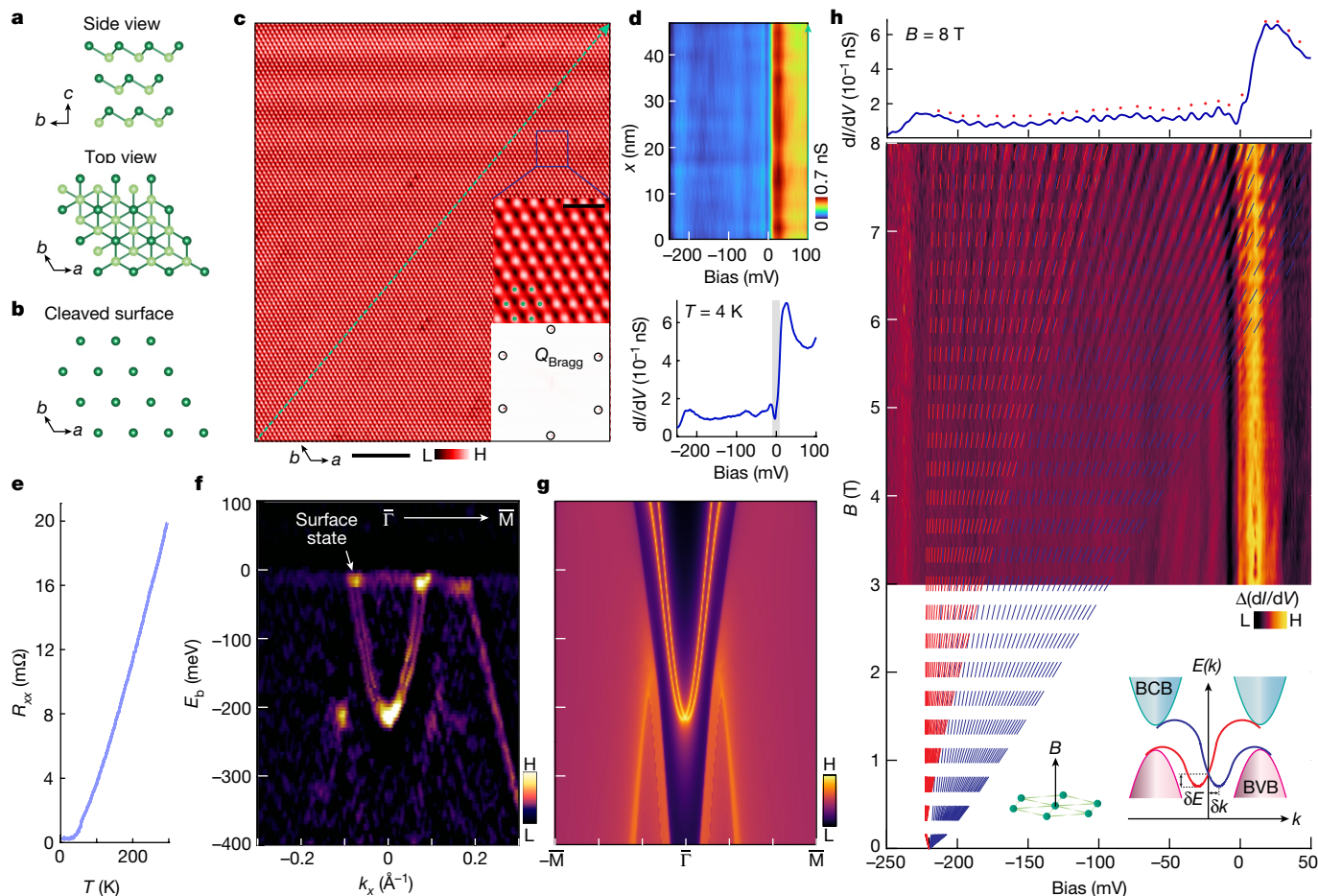


Fig. 1 | Observation of surface state in α -As and its Landau quantization.

a, Top, side view of α -As crystal, constituting a stacking of As bilayers along the c -axis direction. Bottom, top view of the crystal structure showing the As atoms within the bilayer forming a buckled honeycomb lattice. **b**, Cleaved ab plane comprising a triangular lattice. **c**, STM image of the α -As ab plane ($V_{\text{gap}} = 10$ mV and $I_t = 1$ nA). Top inset, magnified, atomically resolved image of the triangular lattice. Bottom inset, Fourier transform of the topographic image revealing sharp Bragg peaks corresponding to the triangular lattice. Here, the a and b axes represent two symmetry equivalent axes that are rotated by 120° with respect to one another. The axis direction illustrated here is consistently maintained throughout the manuscript to designate these axes. H and L labels in the colour bar denote high and low scale, respectively. **d**, Large-scale spectroscopic line cut of the surface, taken at $T = 4$ K. The corresponding location is marked on the topographic image in **c** with a dotted green line. The direction of the scan is marked with an arrow. The averaged dI/dV , shown at the bottom, reveals a soft gap (reduced spectral weight) near the Fermi energy. Tunnelling junction set-up: $V_{\text{set}} = 100$ mV, $I_{\text{set}} = 0.5$ nA and $V_{\text{mod}} = 0.5$ mV. **e**, Resistance as a function of the temperature measured in a bulk α -As crystal with the contacts placed on the ab plane. Consistent with the presence of a

metallic surface state, the resistance decreases as the sample is cooled down. **f**, Second derivative (curvature) of the energy–momentum cut along the $\Gamma \rightarrow \bar{M}$ direction of the surface Brillouin zone (Extended Data Fig. 1a), obtained from photoemission spectroscopy on the cleaved (111) surface (ab plane). The spectra are acquired using 22 eV, linear-horizontally polarized light. The topological surface state is marked by the white arrow. The small Rashba splitting is visualized in the curvature plot. **g**, Calculated surface bands connecting the bulk conduction and valence bands with Rashba-like features, depicted as bright orange curves projected onto the (111) surface (ab plane). **h**, Top, averaged dI/dV spectrum under $B = 8$ T applied perpendicularly to the cleaved surface, exhibiting intense modulation in differential conductance due to Landau quantization. Bottom, Landau fan diagram of α -As obtained with tunnelling spectroscopy. Two sets of Landau fans, corresponding to the Rashba-split surface state, are visible. The red and blue dashed lines denote a fit to the Rashba-split, up- and down-spin Landau levels, respectively. Left inset, magnetic field applied perpendicularly to the triangular As lattice. Right inset, schematic depiction of Rashba-split bands connecting the bulk conduction bands (BCB) and bulk valence bands (BVB). Tunnelling junction set-up: $V_{\text{set}} = 50$ mV, $I_{\text{set}} = 0.5$ nA and $V_{\text{mod}} = 0.5$ mV. Scale bar, 5 nm (**c**) and 1 nm (inset of **c**).

(1) the step-edge scattering does not vanish at finite momentum and (2) the edge dI/dV peaks are associated with singularities of the density of states at the top and bottom of the edge bands.

Next, we explored step edges with different geometric configurations. We identified two bilayer step-edge geometries along the a axis, as shown in the topographic images in Fig. 3a,b. The bilayer step edge in Fig. 3a exhibits a pronounced step-edge state manifesting as a dI/dV peak at $V \simeq -5$ mV (dI/dV maps in Fig. 3a and spectroscopy in Fig. 3c), which resembles its monolayer counterpart. The dispersion of the bilayer step-edge state is shown in Extended Data Fig. 5. We observe a single prominent scattering branch that is qualitatively like that of the monolayer step-edge state in Fig. 2h. In sharp contrast, the dI/dV

spectrum taken on the step edge in Fig. 3b (dI/dV maps in Fig. 3b and spectroscopy in Fig. 3c) features a suppressed spectral weight near the Fermi energy. We can understand this discrepancy by noting that the two step-edge geometries shown in Fig. 3a,b are not related to each other by any crystalline symmetry. In Fig. 3a, the sample extends to the left of the step edge, whereas in Fig. 3b, it extends to the right. Correspondingly, even though both step edges are aligned along the same crystal axis, they do not exhibit the same electronic structure (monolayer step edges are demonstrated in Extended Data Fig. 6). This situation is reminiscent of the hinge states in higher-order topological insulators, which appear only on alternating edges along the same axis, as, for instance, seen in bismuth⁴⁴. Interestingly, however, a pure

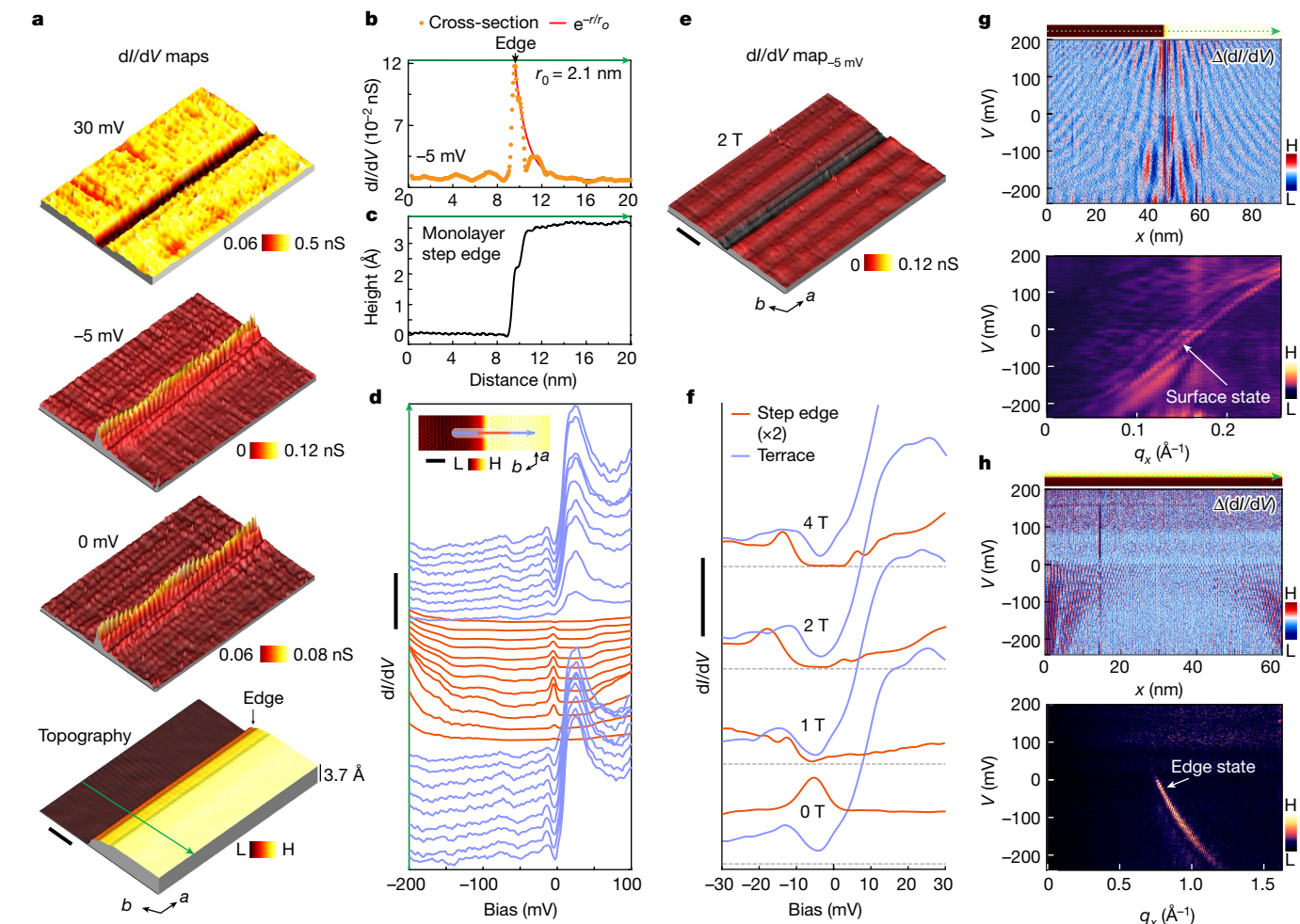


Fig. 2 | Observation of topological step-edge state in a monolayer step edge. **a**, dI/dV maps at different bias voltages (corresponding topography is shown in the bottom panel) around a monolayer step edge parallel to the a -axis direction. **b**, Intensity distribution of differential conductance taken at -5 mV around the step edge. The corresponding location is marked on the topographic image in **a** with a green line. The direction of the scan is marked with an arrow. The red curve shows the exponential fitting of the decay of the state away from the step edge. The fitted decay length is 2.1 nm. **c**, Corresponding height profile, taken perpendicular to the a -axis direction. **d**, Tunnelling spectra, revealing a soft gap away from the step edge and a pronounced in-gap state on the step edge. Orange and violet curves represent the differential spectra taken at different positions (marked on the topographic image shown in the inset) at the step edge and away from it, respectively. Spectra are offset for clarity. **e**, dI/dV map at $B = 2$ T ($V = -5$ mV) taken in the same region as in **a** (topography in the bottom image of **a**), exhibiting a suppressed differential conductance along the edge. **f**, Differential spectra at $B = 0, 1, 2$ and 4 T. Orange and violet curves denote the

spectra taken at the step edge and far away from the step edge, respectively. Spectra at different magnetic fields are taken at the same locations and are offset for clarity. Dashed horizontal lines mark the zero dI/dV for different fields. The spectra are presented within the bias range $[-30$ mV, 30 mV]. **g, h**, Line spectroscopies with high spatial and energy resolutions taken perpendicular to a monolayer step edge (**g**) and along the same monolayer step edge (**h**). This monolayer step edge, whose orientation matches that of the step edge shown in **a**, exhibits a clear step-edge state. The top panels depict intensity plots, with green dotted lines marking the corresponding locations on the topographic images (which are shown at the top) and arrows indicating the scan directions. The bottom panels display corresponding one-dimensional Fourier transforms showcasing clear dispersions. Tunnelling junction set-up for dI/dV maps in **a** and **e**: $V_{\text{set}} = 100$ mV, $I_{\text{set}} = 0.5$ nA and $V_{\text{mod}} = 1$ mV. Tunnelling junction set-up for the differential spectra in **d** and **f**: $V_{\text{set}} = 100$ mV, $I_{\text{set}} = 0.5$ nA and $V_{\text{mod}} = 0.5$ mV. Tunnelling junction set-up for the line spectroscopies in **g** and **h**: $V_{\text{set}} = 200$ mV, $I_{\text{set}} = 0.5$ nA and $V_{\text{mod}} = 0.5$ mV. Scale bars, 5 nm (**a, e**), 0.2 nS (**d, f**), 2 nm (**d**, inset).

(non-hybrid) higher-order topological insulator would not exhibit gapless monolayer or bilayer step-edge states, as the step-edge height would need to be thermodynamically large to guarantee gapless hinge states (Extended Data Fig. 7). Moreover, a pure (non-hybrid) strong topological insulator is expected generically to feature only surface states on the plateaus bordering the step edge, rather than well-localized gapless states along the step edges themselves. Below and in the Supplementary Information, we explain how the step-edge states measured in α -As instead result from hybridization between the gapless first-order surface states and the gapped higher-order hinge state precursors. They, therefore, represent an immediate experimental indicator for hybrid topology. Notably, this contrasts with bismuth, for which our ab initio calculations (Supplementary Information section IV) reveal

a gapless edge mode in monolayer bismuth, in agreement with previous experiments²³. Conversely, for monolayer α -As, our ab initio calculations indicate the presence of a pair of gapped edge states (Supplementary Information section IV). The emergence of gapless edge modes in α -As step edges occurs only upon hybridization with the surface states existing in the bulk step-edge geometry.

The hybrid topology is further orchestrated in a triangular pit (Fig. 3d) composed of a bilayer step edge along the a -axis direction and two monolayer step edges along the b axis and rotated by 120° with respect to it. Owing to the same geometric configuration as that of the step edge in Fig. 3a, the bilayer step edge features a pronounced step-edge state (dI/dV maps in Fig. 3d and dI/dV spectrum in Fig. 3e). Note that the bilayer step edge in Fig. 3d has similar electronic

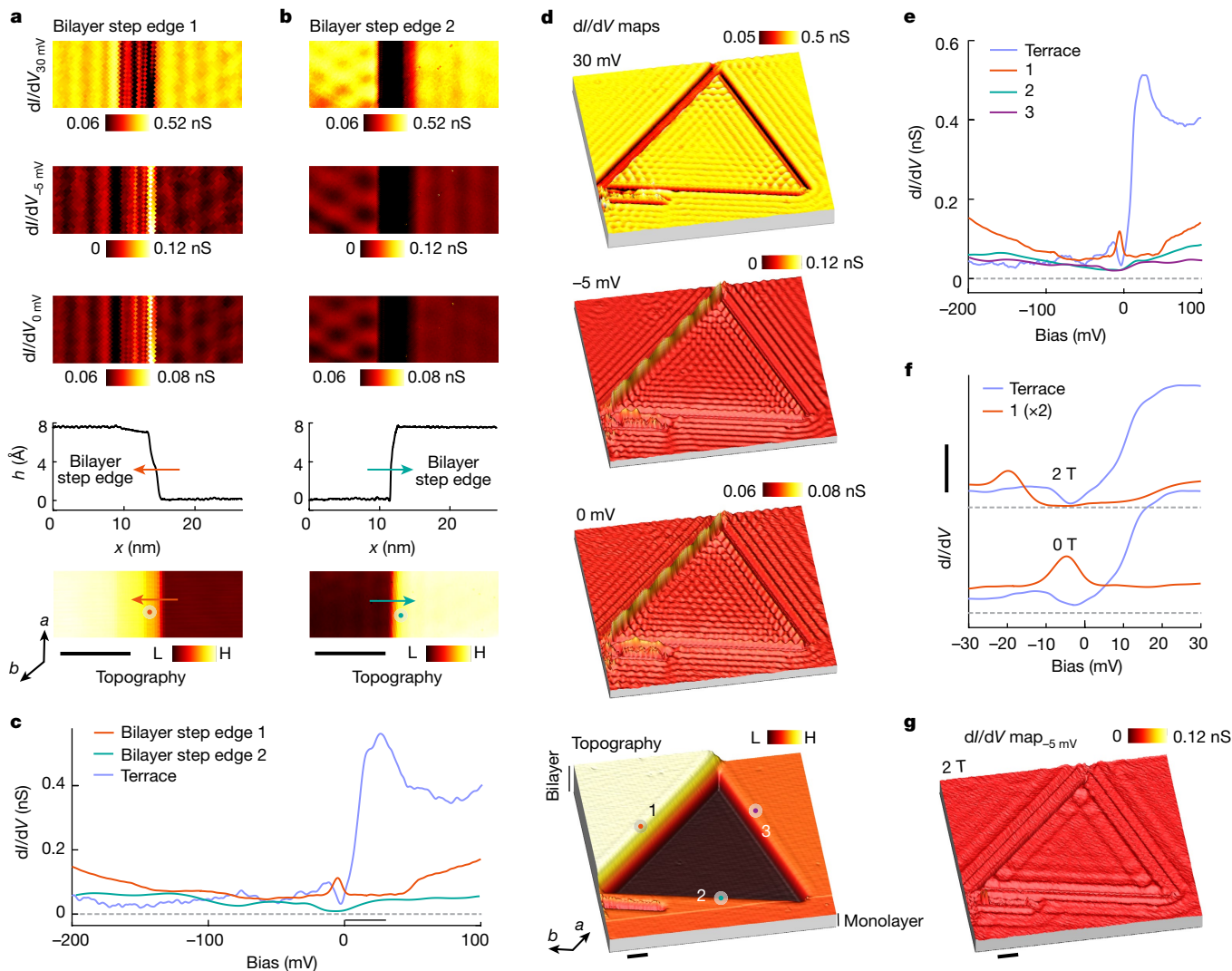


Fig. 3 | Orientation dependence of the step-edge states. **a, b**, Topographic images, height profiles, and the corresponding differential conductance maps around two bilayer step edges: 1 (**a**) and 2 (**b**), as marked. The colour-coded arrows in the topographies and the height profiles indicate the directions from the bottom to the top terraces. **c**, Differential spectra, taken at the bilayer step edge 1 (orange), bilayer step edge 2 (green) and away from the step edges (violet), revealing striking differences between the two step edges. Orange and green dots in the topographic images in **a** and **b** denote the respective positions on the bilayer step edges 1 and 2 where the differential spectra were taken. **d**, Topographic images and the corresponding differential conductance maps around a triangular pit composed of a bilayer step edge (whose orientation is akin to the bilayer step edge 1 in **a**) along the *a* axis of the crystal and two monolayer step edges along the *b* axis and rotated by 120° with respect to it. **e**, Differential spectra taken at the three step edges shown in **d** (a bilayer step

properties as the monolayer step edge in Fig. 2, namely a peak at $V \approx -5$ mV and the emergence of an energy gap as a function of the magnetic field (Fig. 3f). Correspondingly, dI/dV at the step edge becomes substantially suppressed (dI/dV map for $B = 2$ T in Fig. 3g). Intriguingly, however, the monolayer step edges in Fig. 3d, which are oriented along the *b* axis and rotated by 120° with respect to it, do not show an enhancement in dI/dV along the step edge. In fact, as is evident in Fig. 3e, instead of a peak in the dI/dV spectra, they exhibit a suppressed spectral weight near the Fermi energy, pointing to the absence of a step-edge state along these two step edges. Analogous to the absence of step-edge states along certain bilayer (monolayer) orientations, which are clear in Fig. 3b (Extended Data Fig. 6), this finding

edge in orange and two monolayer step edges in green and purple) and away from the step edges (violet). Orange, green and purple dots in the topographic image in **d** denote the respective positions on the bilayer and the two monolayer step edges where the differential spectra were taken. **f**, Differential spectra for $B = 0$ T and 2 T. Orange and violet curves denote the spectra taken at the bilayer step edge in **d** and far away from the step edge, respectively. Spectra at the two magnetic fields are taken at the same locations and are offset for clarity. Dashed horizontal lines mark the zero dI/dV for different fields. The spectra are plotted over a bias range $[-30$ mV, 30 mV]. **g**, dI/dV map at $V = -5$ mV taken on the same region as in **d** (topography in **d** bottom image) for $B = 2$ T. Tunnelling junction set-up for the differential spectra: $V_{\text{set}} = 100$ mV, $I_{\text{set}} = 0.5$ nA and $V_{\text{mod}} = 0.5$ mV. Tunnelling junction set-up for dI/dV maps: $V_{\text{set}} = 100$ mV, $I_{\text{set}} = 0.5$ nA and $V_{\text{mod}} = 1$ mV. Scale bars, 10 nm (**a, b, d, g**), 0.2 nS (**f**).

suggests that one should observe step-edge states at the monolayer step edges along the *b* axis (and axes rotated by 120° with respect to it) when the sample extends in the opposite direction compared to the monolayer step edges in Fig. 3d. Our experimental results in Extended Data Fig. 8 confirm this.

Theoretical calculations

To understand the unusual geometric properties of the step-edge states discussed in the above two paragraphs, we undertook systematic theoretical calculations, which are detailed in the Supplementary Information. We relate the presence of step-edge modes in α -As (Fig. 4a)

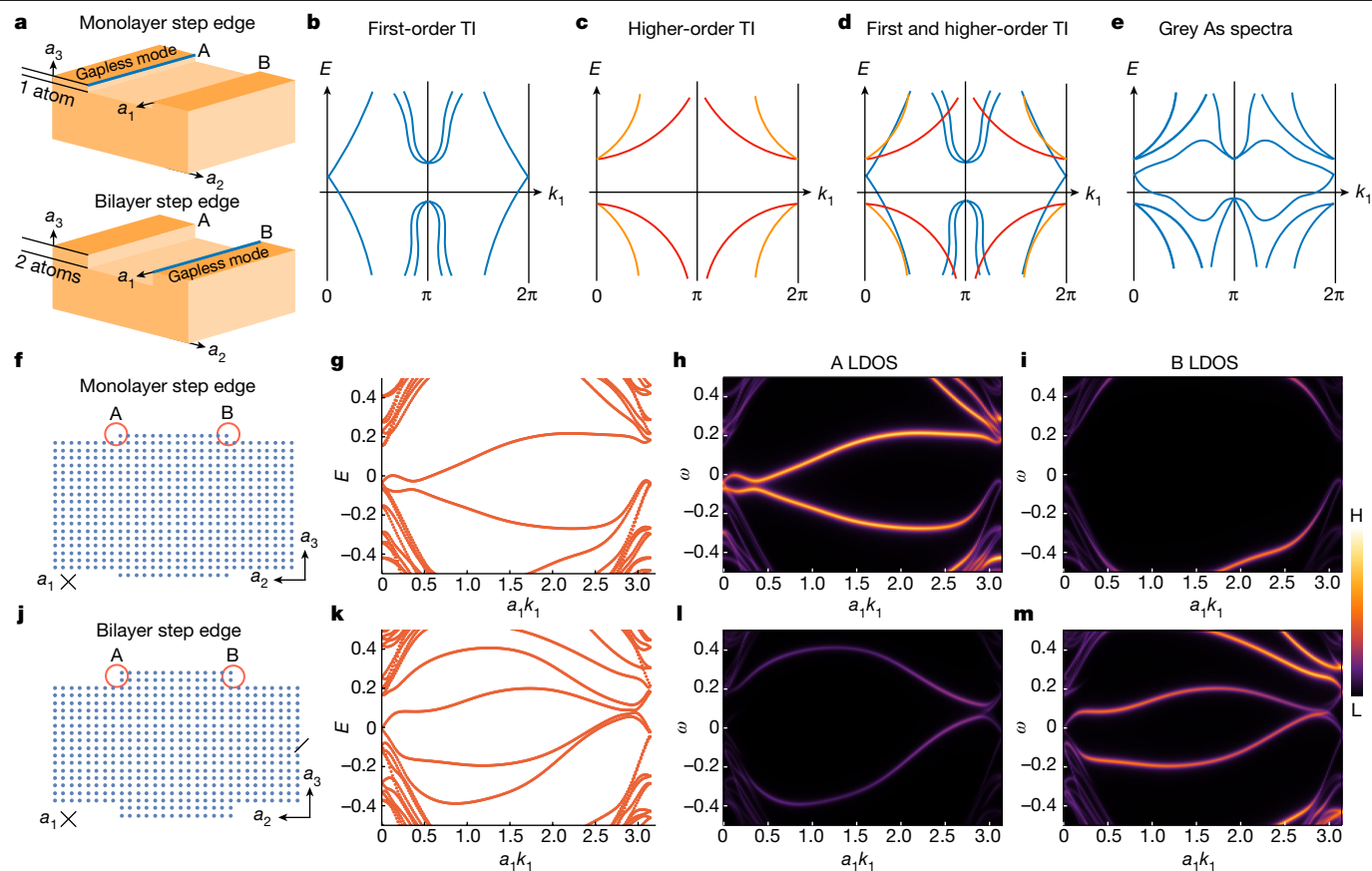


Fig. 4 | Hybrid topology of α -As manifested in step-edge states. **a**, Schematic step-edge states in α -As in a representative geometry preserving the momentum $k_1 \equiv \mathbf{k} \cdot \mathbf{a}_1$. The two types of step edges (A and B) are indicated. **b**, Schematic band structure of a non-hybrid first-order topological insulator (TI) cut into this step-edge geometry. The valence bands were obtained from a trivial insulator by a single band inversion at the three C_3 -related L , L' and L'' points of the Brillouin zone (Extended Data Fig. 1a). Unlike α -As, there is no additional double band inversion that would imply higher-order topology. As derived in the Supplementary Information, the gapless state at $k_1 = 0$ is not localized well at the step edge. **c**, Schematic band structure of a non-hybrid higher-order topological insulator cut into the step-edge geometry shown in **a**. The valence bands were obtained from a trivial insulator by a double band inversion at the Γ point of the Brillouin zone. Unlike α -As, there is no additional single band inversion that would imply first-order topology. There are no gapless modes, but we expect that there are gapped higher-order hinge states that are well localized along either the A or B step edge. **d**, Superimposed spectra from **b** and **c**.

e, The bulk electronic structure of α -As is a combination of the situations shown in **b** and **c**. In the step-edge geometry, this leads to hybridization between the gapless surface states around $k_1 = 0$ and the gapped, localized, step-edge, higher-order, hinge states at finite k_1 , giving rise to gapless and localized step-edge states with an enhanced density of states close to the Fermi level. **f–m**, Step-edge states in a tight-binding system modelling the band topology of α -As. **f**, Monolayer step-edge geometry with k_1 as a conserved crystal momentum. There are two step edges, one of type A and one of type B, on each of the top and bottom surfaces. This is the minimal configuration of step edges that preserves inversion symmetry as well as periodic boundary conditions along the a_2 direction. **g**, Monolayer step-edge dispersion with k_1 using the lattice shown in **f**. The spectrum in the range $k_1 \in [\pi, 2\pi]$ is related by time-reversal symmetry. There is a gapless helical mode with crossing at $k_1 = 0$ (compare with **a**). **h**, Local density of states (LDOS) for the A step edge. **i**, LDOS for the B step edge. **j**, Bilayer step-edge geometry. **k**, Bilayer step-edge dispersion. **l**, LDOS for the A step edge. **m**, LDOS for the B step edge.

to its bulk topology. First-principles calculations predict that α -As is a first-order topological insulator with Dirac-cone surface states¹⁶, but also that it should host higher-order hinge states^{17,18}. We have already discussed the experimental evidence for first-order topology. In terms of the experimental signature of higher-order topology, we observed a pronounced gapless state localized at a six-atomic-layer-thick step edge of a specific orientation, whereas no such state is present in the other orientation (Extended Data Fig. 9e,f,i). In this case, the step-edge height is sufficiently thick to permit well-separated hinge states between the top and bottom hinges. Therefore, the observation of such geometry-dependent hinge states on a thick step edge can be regarded as evidence for the presence of non-trivial second-order topology. Note that we cannot exclude the possibility of hybridization between the edge and surface states, even for higher step edges, if it does not lead to the gapping-out of the step-edge states. However, we emphasize that this does not impact our conclusion, which is the presence of higher-order topology, from the gapless hinge states observed on

high step edges. Furthermore, we show in detail in the Supplementary Information that the presence of gapless states on thin step edges, such as the monolayer and bilayer step edges discussed above, is another unambiguous indicator of higher-order topology. This is because such states would not be present in a non-hybrid first-order topological insulator. To confirm this, we first derive the presence of gapless (helical) step-edge states on general grounds and then corroborate our analysis by an explicit tight-binding model. Although the existence of gapless states in the step-edge geometry relies only on α -As being a (first-order) topological insulator (as illustrated in Fig. 4b), their hybridization with the higher-order hinge states (detailed in Fig. 4c–e), which are finite-size gapped along monolayer and bilayer step edges, localizes them to the step edges and substantially increases their spectral weight around the Fermi level (see Supplementary Fig. 1 and Supplementary Information section IC for details). The resulting electronic structure of the step edge in α -As (Fig. 4e), therefore, hosts a helical pair of gapless states, which are protected to remain gapless by the non-trivial first-order

topology in the presence of time-reversal symmetry but localized along the step edge by the concurrent non-trivial second-order topology. For the tight-binding model, which has the same topological invariants as α -As, we chose idealized monolayer (Fig. 4f) and bilayer (Fig. 4j) geometries that preserve the crystalline inversion symmetry. The resulting band structure features gapless step-edge states along both the monolayer and bilayer step edges, as shown in Fig. 4g,k, respectively. Consistent with the situation in α -As, the states that are closest to the Fermi level prefer one step-edge orientation over another, and the preferred orientation is swapped when going from the monolayer (see Fig. 4h,i for orientation-resolved density of states) to the bilayer (see Fig. 4l,m for the orientation-resolved density of states). Such an even/odd effect in the preferred orientation of the step-edge state persists in three- and four-layer step edges (Extended Data Fig. 9a–d,g,h), which also display geometry-dependent step-edge states.

Conclusion

The combination of theoretical and experimental results presented here clearly indicates that the observed step-edge states in α -As, unlike surface or hinge states, are not expected for either first or higher-order topological insulators separately but only for hybrid materials in which both kinds of band topology are present. Our results reveal the presence of topological step-edge modes along specific geometrical configurations that are compatible with its crystalline symmetries, thus offering a new pathway for engineering topological step-edge conduction along selective crystallographic orientations and advanced quantum techniques. The topological order observed in α -As suggests that it can be used as a platform for exploring quantum information science in future devices. Furthermore, the identification of elemental solids as material platforms, such as antimony hosting a strong band inversion topology⁴⁵ or bismuth hosting a higher-order topology⁴⁴, has led to the substantial development of novel materials that have immensely benefited the field of topological materials. We envision that arsenic, with its unique topology, may serve as a new platform at a similar level for developing novel topological materials and quantum devices that are not at present accessible through bismuth- or antimony-based platforms.

Online content

Any methods, additional references, Nature Portfolio reporting summaries, source data, extended data, supplementary information, acknowledgements, peer review information; details of author contributions and competing interests; and statements of data and code availability are available at <https://doi.org/10.1038/s41586-024-07203-8>.

- Hasan, M. Z. & Kane, C. L. Colloquium: topological insulators. *Rev. Mod. Phys.* **82**, 3045–3067 (2010).
- Qi, X.-L. & Zhang, S.-C. Topological insulators and superconductors. *Rev. Mod. Phys.* **83**, 1057 (2011).
- Hasan, M. Z., Xu, S.-Y. & Bian, G. Topological insulators, topological superconductors and Weyl fermion semimetals: discoveries, perspectives and outlooks. *Phys. Scr.* **2015**, 014001 (2015).
- Grund, S. C., Hanusch, K. & Wolf, H. U. in *Ullmann's Encyclopedia of Industrial Chemistry* (Wiley-VCH, 2005).
- Norman, N. C. *Chemistry of Arsenic, Antimony and Bismuth* (Springer, 1998).
- Zhang, F., Kane, C. L. & Mele, E. J. Surface states of topological insulators. *Phys. Rev. B* **86**, 081303(R) (2012).
- Bernevig, B. A. & Hughes, T. L. *Topological Insulators and Topological Superconductors* (Princeton Univ. Press, 2013).
- Tang, F. et al. Efficient topological materials discovery using symmetry indicators. *Nat. Phys.* **15**, 470–476 (2019).
- Schindler, F. et al. Higher-order topological insulators. *Sci. Adv.* **4**, eaat0346 (2018).

- Benalcazar, W. A., Bernevig, B. A. & Hughes, T. L. Electric multipole moments, topological multipole moment pumping, and chiral hinge states in crystalline insulators. *Phys. Rev. B* **96**, 245115 (2017).
- Song, Z., Fang, Z. & Fang, C. ($d-2$)-dimensional edge states of rotation symmetry protected topological states. *Phys. Rev. Lett.* **119**, 246402 (2017).
- Zhang, F., Kane, C. L. & Mele, E. J. Surface state magnetization and chiral edge states on topological insulators. *Phys. Rev. Lett.* **110**, 046404 (2013).
- Fu, L. & Kane, C. L. Topological insulators with inversion symmetry. *Phys. Rev. B* **76**, 045302 (2007).
- Khalaf, E., Po, H. C., Vishwanath, A. & Watanabe, H. Symmetry indicators and anomalous surface states of topological crystalline insulators. *Phys. Rev. X* **8**, 031070 (2018).
- Kruthoff, J. et al. Topological classification of crystalline insulators through band structure combinatorics. *Phys. Rev. X* **7**, 041069 (2017).
- Zhang, P. et al. Topologically entangled Rashba-split Shockley states on the surface of grey arsenic. *Phys. Rev. Lett.* **118**, 046802 (2017).
- Bradlyn, B. et al. Topological quantum chemistry. *Nature* **547**, 298–305 (2017).
- Vergniory, M. G. et al. A complete catalogue of high-quality topological materials. *Nature* **566**, 480–485 (2019).
- Vergniory, M. G. et al. All topological bands of all nonmagnetic stoichiometric materials. *Science* **376**, eabg9094 (2022).
- Tang, S. et al. Quantum spin Hall state in monolayer 1T'-WTe₂. *Nat. Phys.* **13**, 683–687 (2017).
- Yin, J.-X., Pan, S. H. & Hasan, M. Z. Probing topological quantum matter with scanning tunnelling microscopy. *Nat. Rev. Phys.* **3**, 249 (2021).
- Yang, F. et al. Spatial and energy distribution of topological edge states in single Bi(111) bilayer. *Phys. Rev. Lett.* **109**, 016801 (2012).
- Drozdov, I. K. et al. One-dimensional topological edge states of bismuth bilayers. *Nat. Phys.* **10**, 664–669 (2014).
- Pauly, C. et al. Subnanometre-wide electron channels protected by topology. *Nat. Phys.* **11**, 338–343 (2015).
- Wu, R. et al. Evidence for topological edge states in a large energy gap near the step edges on the surface of ZrTe₅. *Phys. Rev. X* **6**, 021017 (2016).
- Li, X.-B. et al. Experimental observation of topological edge states at the surface step edge of the topological insulator ZrTe₅. *Phys. Rev. Lett.* **116**, 176803 (2016).
- Wang, Z. et al. Topological edge states in a high-temperature superconductor FeSe/SrTiO₃(001) film. *Nat. Mater.* **15**, 968–973 (2016).
- Sessj, P. et al. Robust spin-polarized midgap states at step edges of topological crystalline insulators. *Science* **354**, 1269–1273 (2016).
- Peng, L. et al. Observation of topological states residing at step edges of WTe₂. *Nat. Commun.* **8**, 659 (2017).
- Liu, S. et al. Experimental observation of conductive edge states in weak topological insulator candidate HfTe₅. *APL Mater.* **6**, 121111 (2018).
- Ugeda, M. M. et al. Observation of topologically protected states at crystalline phase boundaries in single-layer WSe₂. *Nat. Commun.* **9**, 3401 (2018).
- Liu, R. Z. et al. Experimental observations indicating the topological nature of the edge states on HfTe₅. *Chin. Phys. Lett.* **36**, 117301 (2019).
- Yin, J. X. et al. Quantum-limit Chern topological magnetism in TbMn₆Sn₆. *Nature* **583**, 533 (2020).
- Shumiya, N. et al. Evidence of a room-temperature quantum spin Hall edge state in a higher-order topological insulator. *Nat. Mater.* **21**, 1111–1115 (2022).
- Miller, D. L. et al. Observing the quantization of zero mass carriers in graphene. *Science* **324**, 924–927 (2009).
- Feldman, B. E. et al. Observation of a nematic quantum Hall liquid on the surface of bismuth. *Science* **354**, 316–321 (2016).
- Hanaguri, T., Igarashi, K. & Kawamura, M. Momentum-resolved Landau-level spectroscopy of Dirac surface state in Bi₂Se₃. *Phys. Rev. B* **82**, 081305 (2010).
- Okada, Y., Serbyn, M., Lin, H. & Walkup, D. Observation of Dirac node formation and mass acquisition in a topological crystalline insulator. *Science* **341**, 1496–1499 (2013).
- König, M. et al. The quantum spin Hall effect: theory and experiment. *J. Phys. Soc. Jpn* **77**, 031007 (2008).
- Shi, Y. et al. Imaging quantum spin Hall edges in monolayer WTe₂. *Sci. Adv.* **5**, eaat8799 (2019).
- Dominguez, F. et al. Testing topological protection of edge states in hexagonal quantum spin Hall candidate materials. *Phys. Rev. B* **98**, 161407(R) (2018).
- Song, Z. et al. First principle calculation of the effective Zeeman's couplings in topological materials. In *Memorial Volume for Shoucheng Zhang* Ch. 11, 263–281 (2021).
- Fu, Y. S. et al. Observation of Zeeman effect in topological surface state with distinct material dependence. *Nat. Commun.* **7**, 10829 (2016).
- Schindler, F. et al. Higher-order topology in bismuth. *Nat. Phys.* **14**, 918–924 (2018).
- Teo, J. C. Y., Fu, L. & Kane, C. L. Surface states and topological invariants in three-dimensional topological insulators: Application to Bi_{1-x}Sb_x. *Phys. Rev. B* **78**, 045426 (2008).

Publisher's note Springer Nature remains neutral with regard to jurisdictional claims in published maps and institutional affiliations.

Springer Nature or its licensor (e.g. a society or other partner) holds exclusive rights to this article under a publishing agreement with the author(s) or other rightsholder(s); author self-archiving of the accepted manuscript version of this article is solely governed by the terms of such publishing agreement and applicable law.

© The Author(s), under exclusive licence to Springer Nature Limited 2024

Methods

α -As single-crystal growth

Single crystals of α -As were grown by the chemical vapour transport method. First, the As (PPM pure metals, 99.999995%) was filled into an evacuated quartz ampoule and subsequently heated up to 1,073 K for 48 h. The polycrystalline As pellets were ground and placed into the quartz ampoule along with iodine shots (2 mg cm^{-3}) as the transport agent. The quartz ampoule was then evacuated and sealed under vacuum. The quartz ampoule was kept under a temperature zone with a gradient ranging from 1,073 K (growth zone) and 1,173 K (source zone) for 5 days, and subsequently cooled down to room temperature at a rate of 50 K h^{-1} . Large two-dimensional high-quality α -As crystals of dimensions up to 8 mm were obtained at the low-temperature zone.

Scanning tunnelling microscopy

Single crystals were cleaved mechanically in situ at $T = 77 \text{ K}$ under ultra-high vacuum conditions (less than $5 \times 10^{-10} \text{ mbar}$) and then immediately inserted into the microscope head, which was already at the ^4He base temperature (4.2 K). More than 20 single crystals were cleaved for this study. For each cleaved crystal, we explored surface areas over $10 \mu\text{m} \times 10 \mu\text{m}$ to search for atomically flat surfaces. Topographic images in this work were taken in the constant current mode. Tunneling conductance spectra were obtained with a commercial Ir/Pt tip (annealed in an ultra-high vacuum and then characterized with a reference sample) using standard lock-in amplifier techniques with a lock-in frequency of 977 Hz and tunnelling junction set-ups as indicated in the corresponding figure captions. The magnetic field was applied through a zero-field cooling method. To acquire the field-dependent tunnelling conductance map, we first withdrew the tip away from the sample and then slowly ramped the field up to the desired value. Then we returned the tip to the sample, found the same atomic area and performed spectroscopic mapping at this magnetic field.

ARPES measurements

The ARPES measurements shown in Extended Data Figs. 1d–g and 2d were performed at the beamline BL21_ID of National Synchrotron Light Source II. The samples were cleaved and measured at $T = 10 \text{ K}$. For the Fermi surface measurements, the energy and angle resolution were below 20 meV and 0.2° , respectively. For the energy–momentum cuts, the energy and momentum resolutions were below 8 meV and 0.2° , respectively.

The ARPES data shown in Fig. 1f and Extended Data Fig. 1h,i were taken at beamline BL-13U of the National Synchrotron Radiation Laboratory, Hefei, which is equipped with a Scienta Omicron DA30L electron analyser. The incident light ($h\nu = 22 \text{ eV}$) was horizontally polarized. The energy and angular resolutions were below 20 meV and 0.3° , respectively. The samples were cleaved in situ at around $T = 12 \text{ K}$ under a vacuum better than $6 \times 10^{-11} \text{ mbar}$.

First-principles calculations

Electronic structure calculations were performed with density functional theory using the Vienna Ab initio Simulation Package (VASP)^{46,47}. The general gradient approximation functional was used to treat the exchange–correlation effect⁴⁸. A plane-wave cutoff of 500 eV was used in all calculations. The relativistic effect of spin–orbit coupling was included self-consistently in the calculations. The structural parameters were taken from experimental data. An energy tolerance of 10^{-8} eV was used. We performed the calculations using $18 \times 18 \times 14$ k points centred at the Γ point with 4,536 k points in the Brillouin zone. We extracted the real-space, tight-binding, Hamiltonian with an atom-centred Wannier function with (s , p and d)-As orbital projection using the wannier90 code⁴⁹. We constructed our model using a real-space, tight-binding, Hamiltonian to study the topological properties using the Wannier

tools package⁵⁰. The Fermi surface was calculated on an interpolated mesh of $180 \times 180 \times 140$ using the wannier90 code and visualized with Xcrysden (refs. 51,52).

Energy–momentum diagrams

Here we discuss the bulk and surface band structure of α -As in light of our first-principles calculations and photoemission spectroscopy data. The bulk and the (111) surface Brillouin zones are displayed in Extended Data Fig. 1a. Extended Data Fig. 1b captures the bulk bands and shows a semimetal feature at the Fermi energy. That is, both the bulk valence and bulk conduction bands cross the Fermi energy, whereas there is a gap between the two throughout the Brillouin zone.

Next, we turn to the electronic band structure projected onto the (111) surface (ab plane). As shown in Extended Data Fig. 1c, the As (111) surface features a pair of parabolic bands, which split along the $\bar{\Gamma} \rightarrow \bar{M}$ direction but it stays degenerate at the point $\bar{\Gamma}$. Note that these two parabolic bands form two concentric Fermi surfaces enclosing the point $\bar{\Gamma}$ (Extended Data Fig. 2c). Consistent with previous work on α -As (ref. 14), these two parabolic bands signal the Rashba-split surface state. Upon inspecting the spin textures of the corresponding bands (Extended Data Fig. 1c, right panel), we found that the two bands are spin polarized and of opposite spins, lending further credence to the Rashba-like nature of these surface bands.

Having discussed the bulk and surface bands of α -As from the lens of first-principles calculations, we now proceed to experimentally probe these bands. Extended Data Fig. 1d–f shows the ARPES bulk band structure measured with synchrotron radiation. Although the energy–momentum cuts (cuts 1–3 as marked in the bulk Brillouin zone) do not completely cover the complete Brillouin zones, they still bring out the salient features of the electronic structure of α -As near its Fermi energy. Extended Data Fig. 1d–f also contains the calculated energy–momentum diagrams along the cuts 1–3 to facilitate a comparison between first-principles calculations and photoemission experiments. Note that our synchrotron photoemission spectroscopy captures only the occupied side of the band structure. As displayed in Extended Data Fig. 1d, consistent with the first-principles results, we observe a valence band with the band maximum (near the point T) below the Fermi energy. On the other hand, the energy–momentum cut encompassing the point $\bar{\Gamma}$ (Extended Data Fig. 1e) features no band, matching the first-principles calculations as well. Lastly, examining the energy–momentum cut along L (Extended Data Fig. 1f), we found that both the valence (magenta bands in the corresponding first-principles results) and conduction bands (cyan bands in the corresponding first-principles results) cross the Fermi energy. Furthermore, the spectral intensity stemming from the conduction band crossing the Fermi energy (cyan bands in the corresponding first-principles results) indicates a band minimum at the L point. All these properties of the band structure visualized in the photoemission energy–momentum cuts are in excellent agreement with the first-principles calculations.

Upon further inspection of the photoemission results presented in Extended Data Fig. 1d–f, we found that parabolic-shaped band intensities are present and centred at $k = 0$ in all three energy–momentum cuts. Extended Data Fig. 1g, which depicts the photon energy dependence, further highlights the ubiquity of this band intensity throughout k_z (see the spectral intensities near $k_x \approx \pm 0.05 \text{ \AA}$, which are present in the entire range of photon energies used in our experiments). This finding is consistent with the presence of the Rashba-like surface state¹⁴.

To carefully probe the surface state in our photoemission spectroscopy experiments, we used a lower photon energy (22 eV) and focused on a smaller energy range. Along $\bar{\Gamma} \rightarrow \bar{M}$, we observed sharp, parabolic bands whose bottoms lie at $E \approx -215 \pm 20 \text{ meV}$ and close to $k = 0$ (Extended Data Fig. 1h; also shown in Fig. 1f). Extended Data Fig. 1i presents the dispersion of the surface state extracted from our experimental data along with parabolic fits. Like the experimental bulk bands, the surface bands exhibit consistency with the first-principles results

presented in Extended Data Fig. 1c (also depicted in Fig. 1g). We found that the separation between the Rashba-split surface bands is very small ($\Delta k \approx 0.006 \pm 0.0025 \text{ \AA}^{-1}$). This value of Rashba splitting is in excellent agreement with our first-principles results (see Supplementary Table 1 for a quantitative comparison) as well as with previous photoemission work¹⁶, which used a high-resolution 6 eV laser as a light source and reported a similar value of $\Delta k \approx 0.0054 \text{ \AA}^{-1}$.

In summary, our comprehensive and high-quality photoemission spectroscopy measurements of the bulk states of α -As demonstrate that the first-principles calculation accurately captures the bulk states and validates our first-principles based tight-binding modelling approach. Importantly, we also confirmed the nature of the surface state of the Rashba state by examining the photon energy dependence of our measurements. Furthermore, our analysis of the surface-state spectrum, which is also reproduced well by first-principles calculations, and the demonstration of the small but well-resolved Rashba splitting in photoemission experiments using synchrotron radiation not only confirmed the previous laser-based photoemission spectroscopy results but also provide a reference point for interpreting the Landau fan diagram and quasiparticle interference obtained from STM measurements of the same sample.

Fermi surface mapping

Here, we discuss our findings from the Fermi surface mapping based on first-principles calculations (Extended Data Fig. 2a–c) and photoemission spectroscopy (Extended Data Fig. 2d). As illustrated in Extended Data Fig. 2a,b, the bulk Fermi surface in α -As contains a hole-like (α) and an electron-like (β) pocket, both of which are threefold symmetric. Inclusion of the Rashba-like surface states adds two concentric ring-shaped Fermi pockets centred at $k = 0$. Extended Data Fig. 2c shows the resulting Fermi surface projected on the α -As (111) surface. Extended Data Fig. 2d depicts the Fermi surface sheets obtained from photoemission spectroscopy of the cleaved As (111) surface. The shape of the experimentally obtained Fermi surfaces broadly matches our first-principles results. Furthermore, photoemission spectroscopy measurements confirmed the presence of the three Fermi pockets. The ring-shaped pocket centred around $k = 0$ (Extended Data Fig. 2d) is associated with the Fermi pockets stemming from the Rashba-like surface states.

Extended STM data

Quasiparticle interference experiment. Our systematic spectroscopic imaging of the As ab plane is presented in Extended Data Fig. 3. We collected differential conductance maps at different bias voltages over a large area. Thanks to the scattering of quasiparticles on the surface, the maps show real-space patterns, which vary as a function of bias (Extended Data Fig. 3a). We obtained the quasiparticle interference data by taking the Fourier transform of the dI/dV maps. At $V > -250$ mV, there was a ring-shaped signal centred at $q = 0$. The radius of the ring-shaped pattern increased as the bias was raised from -250 mV, and the pattern was clearly visible up to $V = 150$ V. At $V = 100$ mV, a sixfold-symmetric star-shaped pattern was seen inside the ring-shaped pattern, which evolved at higher biases, and eventually, at $V = 200$ mV, only a sixfold-symmetric line-crossing pattern was visualized. These scattering patterns exhibit a qualitative agreement with our calculated quasiparticle interference results that were obtained using the joint density of states method and presented in Extended Data Fig. 3b.

Using the quasiparticle interference data as a function of bias, we obtained the quasiparticle scattering spectrum illustrated in Extended Data Fig. 3c. The spectrum contains several quasiparticle interference branches, the most prominent of which disperses in the form of a parabola, akin to the Rashba-like surface state visualized in the photoemission spectroscopy and first-principles calculations (Fig. 1f,g). Furthermore, the energy location of the scattering branch bottom matches the energy of the surface band bottom (Fig. 1f,g).

Therefore, it is fair to say that the parabolic scattering branch in Extended Data Fig. 3b stems from the Rashba-like surface state. Note that the Rashba-split band bottoms are separated only in the momentum direction (see the first-principles results in Fig. 1g), which is why our quasiparticle spectrum, which is not sensitive to momentum, cannot resolve it. The observed quasiparticle scattering spectrum qualitatively matches the quasiparticle spectrum computed using the joint density of states method, which is presented in Extended Data Fig. 3d. Additionally, we provide a quantitative comparison of the quasiparticle interference spectrum with the band structure obtained from photoemission spectroscopy and first-principles calculations in Supplementary Table 1.

Mapping the Landau fan diagram. Here, we discuss the measurements of the tunnelling spectrum under an applied magnetic field and the mapping out of the Landau fan. Note that mapping the Landau fan through tunnelling experiments is non-trivial, and there have only been a few successful examples in the world of quantum materials, including ultra-clean materials such as graphene³⁵, bismuth (ref. 36), Bi_2Se_3 (ref. 37), PbSnSe (ref. 38) and TbMn_6Sn_6 (ref. 33). Here, in α -As, as illustrated in Fig. 1d, the zero-field spectrum is spatially homogeneous. Extended Data Fig. 4a is an intensity plot of the tunnelling differential conductance over a large region when the α -As sample was subjected to an 8 T magnetic field along the c axis. Compared to the $B = 0$ data, the tunnelling spectra at 8 T show dramatic changes with the emergence of a series of intensity peaks indicative of a series of states that are widely distributed in energy (Extended Data Fig. 4b). The appearance of such states signals Landau quantization. The Fourier transform plot revealed that the spectrum contains two nearby frequencies (Extended Data Fig. 4c), hinting at the presence of two sets of Landau fans.

To better understand the Landau quantization, we map its fan diagram in Fig. 1h by slowly ramping up the magnetic field. Mapping the Landau fan is particularly useful in extracting precise band structure information. We highlight several key features in the Landau fan diagram of α -As below.

Focusing on the Landau fans in the magnetic field range 3 to 8 T, we found that the Landau fans exhibit a reasonably linear dispersion as a function of the magnetic field. (Note that at low magnetic fields, the Landau fans are not clearly visible, possibly because of thermal broadening. Therefore, for our analysis, we used the data above 3 T). This is consistent with the Landau fans being formed within parabolic bands.

Further examination revealed that the Landau fan diagram features two sets of electron-type Landau fans. To understand this, we analytically investigated the Landau quantization stemming from the Rashba surface states of α -As, which can be described in a nearly-free-electron band dispersion¹⁶,

$$H = \frac{1}{2m} (P_x^2 + P_y^2) \sigma_0 + \frac{g_n}{2} \mu_B B \sigma_z + \alpha (\sigma_x P_y - \sigma_y P_x), \quad (1)$$

where σ_0 is the identity matrix and B denotes the homogeneous magnetic field perpendicular to the plane of motion, which can be expressed as

$$\mathbf{B} = (0, 0, B), \quad \mathbf{A}(x, y) = \frac{B}{2} (-y, x). \quad (2)$$

In the presence of a magnetic field, the set of momentum operators is

$$\mathbf{P} = -i\hbar\nabla + e\mathbf{A}. \quad (3)$$

Here we can define creation and annihilation operators:

$$a^\dagger = \frac{1}{\sqrt{2e\hbar B}} (P_x + iP_y), \quad a = \frac{1}{\sqrt{2e\hbar B}} (P_x - iP_y). \quad (4)$$

Then the momentum operators can be expressed in terms of the creation and annihilation operators:

$$P_x = \sqrt{\frac{\hbar eB}{2}} (a^\dagger + a), \quad P_y = \sqrt{\frac{\hbar eB}{2}} (a - a^\dagger) i. \quad (5)$$

Therefore, we can rewrite equation (1) as

$$H = \hbar\omega_c \left(a^\dagger a + \frac{1}{2} \right) \sigma_0 + \frac{g_n}{2} \mu_B B \sigma_z + \sqrt{\frac{2eB}{\hbar}} \alpha \begin{pmatrix} 0 & ia \\ -ia^\dagger & 0 \end{pmatrix}. \quad (6)$$

The first term represents the Landau levels for a two-dimensional electron gas, the second term denotes the Zeeman energy and the third term is the Rashba spin-coupling term. Next, we define a basis that contains only the two spin states $\{|N, \uparrow\rangle, |N+1, \downarrow\rangle\}$. The Hamiltonian in this basis is

$$H = \hbar\omega_c (N+1) \sigma_0 - \sqrt{\frac{2eB}{\hbar}} \alpha \sqrt{N+1} \sigma_y + \left(\frac{g_n}{2} \mu_B B - \frac{1}{2} \hbar\omega_c \right) \sigma_z. \quad (7)$$

Finally, we can get all the eigenvalues of the Rashba states in a perpendicular magnetic field:

$$E_{N\pm} = \hbar\omega_c \left(N + \frac{1}{2} \pm \frac{1}{2} \right) \mp \frac{1}{2} \sqrt{(\hbar\omega_c - g_n \mu_B B)^2 + 8\alpha^2 \frac{eB}{\hbar} \left(N + \frac{1}{2} \pm \frac{1}{2} \right)} \quad (8)$$

Here $\omega_c = eB/m^*$, m^* is the effective mass, α is the strength of Rashba effect, g_n is the effective g factor, μ_B is the Bohr magneton, N denotes the Landau levels and $+$ ($-$) represents the spin up (down) state. Importantly, the terms ‘spin up’ and ‘spin down’ used in this context are idiomatic and simply refer to two sets of electronic structures with opposite spin directions, without denoting specific directions. This phenomenon of Rashba-like electronic states generating two sets of Landau fans under a perpendicular magnetic field has been observed in various two-dimensional systems, including magic-angle bilayer graphene⁵³ and few-layer black arsenic⁵⁴. The underlying physical mechanism of this phenomenon is that the Zeeman term induced by the magnetic field opens an energy gap at the crossing point of the Rashba electronic states (second term in equation (8)). This leads to the Rashba electronic states splitting into two independent electronic states⁵⁵.

Existing photoemission results for α -As suggest that the Rashba states should exhibit nearly-free electron behaviour¹⁶. Therefore, the effective g factor can be set as $g_n = 1.00$, which is corroborated in ref. 56. (Note that the g factor associated with the Rashba surface state is different from the g factor that we obtained from the field-dependent edge spectra in Fig. 2). Next, we fitted the effective mass (m^*) and Rashba effect (α) to calculate the Landau fan. By fitting m^* and α based on the experimentally obtained Landau fan diagram we obtained:

Effective mass $m^* \simeq 0.11m_e$.

Rashba strength $\alpha \simeq 0.6 \text{ eV \AA}$.

Our photoemission results suggest that $\delta k \simeq 0.006 \text{ \AA}^{-1}$. Therefore, a Rashba strength $\alpha = 2\delta E/\delta k \simeq 0.6 \text{ eV \AA}$ leads to $\delta E \simeq 1.8 \text{ meV}$. This is reasonable based on our photoemission results for the surface states. Based on the above fitted parameters, we obtained two sets of Landau fans, marked in red (up spin) and blue (down spin) in Fig. 1h, whose origin can be traced to approximately -22 meV . (Note that the linear fits of the Landau bands do not intersect the horizontal axis at the same point because of the Rashba spin splitting). Importantly, this energy position matches the band bottom of the Rashba-like surface state obtained from a series of techniques, namely photoemission spectroscopy (Fig. 1f), quasiparticle interference (Extended Data Fig. 3b) and first-principles calculations (Fig. 1g). This observation leads us to conclude that the Landau fans in α -As arise from the Rashba-like surface state.

The Landau fan diagram also provides information about the Fermi surface. Taking a line cut at the Fermi energy, we obtained the

field-dependent tunnelling differential conductance data depicted in Extended Data Fig. 4d. The data exhibit $1/B$ periodic oscillations, resulting from Landau quantization of the two-dimensional electronic bands. Replotting the data as a function of $1/B$ and then taking the Fourier transform renders two sharp peaks, at 175 and 187 T, as shown in the Extended Data Fig. 4e. These two peaks denote the Fermi surface area (in the units of cyclotron frequency) of the two electron-like Fermi pockets stemming from the Rashba-split surface state. Extended Data Fig. 4f schematically depicts the Rashba Fermi surface containing two concentric ring-shaped pockets. Here in α -As, the areas of the two ring-shaped Fermi pockets are 175 T (inner ring-shaped pocket) and 187 T (outer ring-shaped pocket) in the units of cyclotron frequency. Note that the two frequencies (in the area of both Fermi pockets) are fairly similar. Consequently, the possible crossings between the two sets of Landau fans are not pronounced in the fan diagram shown in Fig. 1h.

Note that, although we observed well-developed Landau levels in α -As (Fig. 1h), it is a semimetal with a substantially higher carrier density compared to typical semiconductor quantum wells³⁹. Consequently, the magnetic fields employed in our experiments do not suffice to trigger strong quantum Hall edge states, for example, the integer quantum Hall state at Landau-level filling factor 1, at the step edge. The magnetic field essentially opened a gap at the Kramers degeneracy point of the step-edge state. The position of the energy gap in Fig. 2f suggests that the Kramers degeneracy point is at around -5 mV , slightly below the Fermi energy. From our field-dependent data, we estimated that the gap opening rate was approximately meV/T , suggesting a large c -axis Landé g factor of approximately 35 for the edge. Note that the large g factor, which may arise from the orbital contributions⁴², has also been reported in other topological materials^{34,42,43}.

Quasiparticle interference along a bilayer step edge

In this section, we present the quasiparticle interference spectrum of a bilayer step-edge state. Extended Data Fig. 5a depicts energy- and spatially resolved dI/dV spectroscopy along a bilayer step edge with the same orientation as the step edges displayed in Fig. 3a,d. We observed a pronounced ripple-like quantum interference pattern, which, upon one-dimensional Fourier transformation with respect to spatial location, yielded the quasiparticle spectrum along the bilayer step edge. The resulting quasiparticle spectrum is shown in Extended Data Fig. 5b, which visualizes a scattering branch akin to the one shown in Fig. 2h for the monolayer step edge. As with the monolayer step-edge state, this scattering branch was distinct from the one that stems from the surface state, as it occupied a different energy-momentum space.

Orientation dependence of the monolayer step edge

In the main text, we discussed the orientation dependence of the step-edge states using two bilayer step edges (Fig. 3a,b), with both lying along the a axis of the crystal but oriented in opposite directions. These orientations differed not by the crystalline axis but by whether the sample height increased or decreased as we crossed the step edge along a fixed perpendicular direction. The data reveal that the step-edge state preferred one orientation over the other. That is, one step edge harboured a step-edge state (Fig. 3a) whereas the other did not (Fig. 3b). In this section, we show similar data but for two monolayer step edges. Extended Data Fig. 6a,b shows two monolayer step edges of opposite orientations along the a -axis direction, as identified by the topographic images. The monolayer step edge in Extended Data Fig. 6a did not carry a step-edge state (see the dI/dV maps in Extended Data Fig. 6a). Rather, it exhibited a suppressed spectral weight near the Fermi energy, as seen in the spectroscopic data in Extended Data Fig. 6c. In stark contrast, a pronounced step-edge state is seen in the monolayer step edge in Extended Data Fig. 6b. The step-edge state was manifested by a dI/dV peak at $V \simeq -5 \text{ mV}$ (see the dI/dV maps in Extended Data Fig. 6b and spectroscopy in Extended Data Fig. 6c).

Analogous to the situation where the step-edge states are seen only along certain bilayer orientations, here the orientation dependence is also rooted in the fact that the two monolayer step-edge geometries in Extended Data Fig. 6a,b are not related to each other by any crystalline symmetry. In Extended Data Fig. 6a, the sample extends to the left of the step edge, whereas in Extended Data Fig. 6b, it extends to the right. Correspondingly, although the step edges are aligned along the same crystal axis, they did not exhibit the same electronic structure. Furthermore, we make the following two remarks connecting the data in Extended Data Fig. 6 to our observations regarding Figs. 2 and 3. First, the monolayer step edges in Fig. 2a and Extended Data Fig. 6b have the same crystal axis and orientation (the sample extends to the right of the step edge). Consequently, they have a similar electronic structure that hosted a step-edge state. Second, by comparing the orientation dependence of the two bilayer step edges in Fig. 3a,b with the two monolayer step edges shown in Extended Data Fig. 6a,b, we found that the orientation hosting gapless states was swapped when going from the bilayer to the monolayer. Specifically, for bilayer step edges, the step edge where the sample extends to the left of the step edge harboured a step-edge state (Fig. 3a). Conversely, the monolayer step edge where the sample extends to the right of the step edge had a step-edge state (Extended Data Fig. 6b). As discussed in the main text (and later in Methods), such an even/odd effect appears independently of the orientation dependence of the step-edge states and is related to the atomic structure of the step edges, which is determined by the crystal structure of α -As and not by its bulk topology.

Extended theoretical discussion on the step-edge states

See the Supplementary Information for a detailed theoretical discussion of the step-edge states in α -As as well as a derivation of and Hamiltonian matrix for the tight-binding model used in our theoretical calculations.

Here we elaborate on the schematic mechanism linking the step-edge states and hybrid topology that was summarized in Fig. 4b–e. Extended Data Fig. 7 is the analogue of Fig. 4f–m for a tight-binding model of a higher-order topological insulator that lies in the same symmetry class as α -As but which, unlike α -As, does not have non-trivial first-order topology. The resulting step-edge spectra, which are schematically depicted in Fig. 4c, were fully gapped but did contain well-localized hinge-mode precursors that contributed a substantial density of states just away from the Fermi level. On the other hand, the step-edge spectra of a first-order topological insulator (schematically depicted in Fig. 4b) generically featured a helical gapless mode, but this mode—unlike the step-edge mode in the regime modelling α -As that is shown in Fig. 4f–m—is not expected to be well localized or to contribute a substantial density of states around the Fermi level.

Considering the above discussion, we conclude that the hybrid topology of α -As (a simultaneous first- and higher-order topological insulator) is indispensable for the existence of gapless step-edge-localized states near the Fermi level, as schematically depicted in Fig. 4e.

Step-edge states at the monolayer step edges along b and \bar{b} rotated by 120° axes

In Fig. 3d, we show that two monolayer step edges along the b axis and those rotated by 120° with respect to it did not exhibit a step-edge state. Here, in another set of monolayer step edges along the b axis and rotated by 120° with respect to it but oriented exactly opposite to the monolayer step edges in Fig. 3d, we found pronounced step-edge states. Extended Data Fig. 8 spectroscopically visualizes this scenario. As demonstrated in Extended Data Fig. 8c, differential conductance maps taken near the Fermi energy (with the corresponding topographic image shown in Extended Data Fig. 8a) revealed an enhanced spectral weight along the step edges. This observation further highlights the orientation dependence of the step-edge states in α -As.

Step-edge states at three-, four- and six-layer step edges

In this section, we further investigate the orientation dependence of step-edge states by examining three- and four-layer-thick atomic step edges, and we present spectroscopic data for six-layer-thick step edges as an indication of the higher-order topological insulator phase in α -As.

We commence by presenting a spectroscopic study of two trilayer step edges (Extended Data Fig. 9a,b) that lie along the a axis of the crystal but face in opposite orientations. Our dI/dV spectroscopic data and maps revealed that the step edge where the sample extends to the right of the step edge harboured a step-edge state (Extended Data Fig. 9b). In contrast, the step edge where the sample extends to the left of the step edge had no such state (Extended Data Fig. 9a). This orientation dependence is identical to that of the monolayer step edge (Extended Data Fig. 6). Next, we identified two oppositely oriented four-layer-thick step edges along the a -axis direction (Extended Data Fig. 9c,d). Spectroscopic measurements suggest that the four-layer step edges also exhibited an orientation dependence of the step-edge state. Namely, the step edge where the sample extends to the left of the step edge hosted a step-edge state (Extended Data Fig. 9c) whereas the step edge where the sample extends to the right of the step edge featured no step-edge state (Extended Data Fig. 9d). This characteristic of the four-layer step edge is identical to that of the bilayer step edge but opposite to the monolayer (and trilayer) step edges. Thus, the orientation dependence of the step-edge state and the even/odd effect in its preferred orientation are also evident for the three- and four-layer step edges.

We also simulated the three- and four-layer step-edge geometries using our tight-binding model. We again took into account the asymmetry between different step edges and layer heights that is induced by the buckled structure of As monolayers (see Supplementary Information for details). We found gapless helical step-edge states along both the three- and four-layer step edges, with an orientation dependence that mirrored that of one- and two-layer step edges, respectively.

Lastly, we examined two six-layer-thick step edges along the a -axis direction (Extended Data Fig. 9e,f) that are oriented in opposite directions. Consistent with all the examined layer thicknesses, we found that the step-edge state preferred one orientation over the other. The step edge where the sample extends to the left of the step edge hosted a step-edge state (Extended Data Fig. 9e), whereas the step edge where the sample extends to the right of the step edge had no step-edge state (Extended Data Fig. 9f). Notably, the thickness of the six-layer step edge was probably sufficient to allow for well-separated and gapless hinge states between the top and bottom hinges. Because STM is sensitive only to the top hinge, a hinge state that propagates by alternating between the top and bottom hinges would manifest as a step-edge state in one orientation (where the hinge state is located on the top hinge), whereas the absence of a step-edge state would be observed in the opposite orientation (where the hinge state is located on the bottom hinge). Therefore, our observation of such orientation-dependent step-edge states on a thick step edge is evidence for the existence of hinge states within the higher-order topological insulator phase.

Edge geometry of α -As

In this section, we will discuss the asymmetry in the atomic structure of α -As step edges along a certain crystallographic axis and its relation to the even/odd effect observed in the step-edge states. As seen from the side view of the crystal structure depicted in Extended Data Fig. 10a, the two monolayer step edges along the a direction exhibited an asymmetry, with one orientation featuring a sharper step edge. This atomic configuration can be visualized from the top view in the atomically resolved topographic images of the corresponding monolayer step edges shown in Extended Data Fig. 10b,c. Similarly, the bilayer step edges of two different orientations also exhibited an asymmetry, with one orientation featuring a sharper step edge (see Extended Data

Fig. 10d for a schematic side view of the bilayer step edge and Extended Data Fig. 10e,f for the top view visualized by STM). Notably, the orientation with a sharper step edge alternated between the monolayer and bilayer cases. This switching is in accordance with the even/odd effect observed in the step-edge states, in which the step-edge state appears to favour the smoother edge. This preference alternated between opposite orientations as the layer thickness was increased from one to two layers. Such a pattern may indicate a connection between the preferred orientation of the step-edge state and the crystal symmetry. Importantly, although the bulk topology of α -As dictates the presence of step-edge states in one of the two possible step-edge orientations along any given crystallographic axis, it does not determine which particular orientation will host the step-edge state. Here, we found that the crystal structure may play a role in this determination.

Additional data on the step-edge states

Here, we present additional data acquired from a different sample. Extended Data Fig. 10g shows the topography and corresponding spectroscopic maps around a monolayer step edge (along the a axis) taken at $V = -5$ mV. Consistent with the step height and the orientation of the step edge in Fig. 2, we also observed a pronounced step-edge state signalled by enhanced differential conductance at the step edge. Furthermore, in agreement with the field-dependent data in Fig. 2e,f, the dI/dV map taken at $B = 2$ T has suppressed tunnelling conductance at the edge, which is consistent with the nature of the step-edge state being protected by time-reversal symmetry.

Orientation dependence of the step-edge states

It is important to distinguish between the topologically enforced features of the step-edge states and those properties that are not topological but rather arise from the microscopic details of α -As. In particular, along any given direction and for any number of layers terminating at the step edge, the existence of a single, helical, step-edge mode for one fixed orientation (with the sample extending either to the left or right of the step edge) is topologically enforced. However, which orientation is preferred by the step-edge state is not dictated by topology but rather depends on the specific properties of the material. (The same holds for hinge modes in a higher-order topological insulator). To decide which orientation is preferred by the step edge for a given number of layers, thereby explaining the observed even/odd effect, we need to take into account more detailed information about α -As beyond its bulk topological invariants. In fact, the orientation dependence of step-edge states and the associated even/odd effect can be attributed to the asymmetry in the atomic structure between the two orientations of the step edge, which is specific to the crystal structure of α -As (see also ‘Edge geometry of α -As’ in Methods and Supplementary Information). Extended Data Fig. 10 further illustrates this asymmetry by showing the crystal structure and corresponding topographic images of both the monolayer and bilayer step edges. Both the monolayer and bilayer step edges display an asymmetry between the two orientations, with one orientation having a sharper step edge than the other. Interestingly, this preferred orientation alternates between the mono- and bilayer cases, in accordance with the even/odd effect observed in the step-edge states, in which the step-edge state always prefers the smoother edge. In fact, this asymmetry simply arises due to the buckling of the As monolayers, as explained in the Supplementary Information. (Note that we could not isolate the effects of the layer number and the type of buckled atoms from only our experimental data). There, we also provide further schematic illustrations for three- and four-layer step edges to confirm that this purely geometric effect, as well as its associated mode localization, persists for thick step edges. As discussed above, a pure higher-order phase generically has gapped hinge states on a monolayer and bilayer step edge (see also Extended Data Fig. 7). Only in the hybrid case will the step-edge state be a gapless helical state that connects the valence and conductance bands (Fig. 4). Although distinguishing between these

two cases based solely on the observation of step-edge states may be difficult, our ARPES data presented in Fig. 1f, in conjunction with the merging of the surface state into the step-edge state observed in the quasiparticle interference spectra in Fig. 2g,h, suggests that the hybrid interpretation is more appropriate. This observation holds crucial significance for future applications in microelectronics and spintronics utilizing α -As step-edge states, as only gapless helical states enjoy protection from backscattering by time-reversal symmetry.

Data availability

All data needed to evaluate the conclusions in the paper are present in the paper. Additional data are available from the corresponding authors upon reasonable request.

- Hohenberg, P. & Kohn, W. Inhomogeneous electron gas. *Phys. Rev.* **136**, B864 (1964).
- Kresse, G. & Furthmüller, J. Efficient iterative schemes for ab initio total-energy calculations using a plane-wave basis set. *Phys. Rev. B* **54**, 11169 (1996).
- Perdew, J. P., Burke, K. & Ernzerhof, M. Generalized gradient approximation made simple. *Phys. Rev. Lett.* **77**, 3865 (1996).
- Mostofi, A. et al. wannier90: a tool for obtaining maximally-localised Wannier functions. *Comput. Phys. Commun.* **178**, 685 (2008).
- Wu, Q., Zhang, S., Song, H.-F., Troyer, M. & Soluyanov, A. A. WannierTools: an open-source software package for novel topological materials. *Comput. Phys. Commun.* **224**, 405 (2018).
- Kokalj, A. XcrySden—a new program for displaying crystalline structures and electron densities. *J. Mol. Graph. Model.* **17**, 176–179 (1999).
- Kokalj, A. Computer graphics and graphical user interfaces as tools in simulations of matter at the atomic scale. *Comp. Mater. Sci.* **28**, 155–168 (2003).
- Das, I. et al. Symmetry-broken Chern insulators and Rashba-like Landau-level crossings in magic-angle bilayer graphene. *Nat. Phys.* **17**, 710–714 (2021).
- Sheng, F. et al. Rashba valleys and quantum Hall states in few-layer black arsenic. *Nature* **593**, 56–60 (2021).
- Winkler, R. *Spin–Orbit Coupling Effects in Two-dimensional Electron and Hole Systems*, Vol. 191 (Springer, 2003).
- O. Madelung, U. Rössler, M. Schulz (eds.) *Non-Tetrahedrally Bonded Elements and Binary Compounds I* (Springer, 1998).

Acknowledgements M.Z.H. group acknowledges primary support from the US Department of Energy (DOE), Office of Science, National Quantum Information Science Research Centers, Quantum Science Center (at Oak Ridge National Laboratory) and Princeton University, support from the Gordon and Betty Moore Foundation for scanning tunneling microscopy instrumentation and theoretical work (Grant No. GBMF9461) and support from the DOE under the Basic Energy Sciences (DOE-BES) programme for theoretical work and photoemission spectroscopy (Grant No. DOE/BES DE-FG-02-05ER46200). R.I. acknowledges support from the Foundation for Polish Science through the international research agendas programme co-financed by the European Union within the smart growth operational programme and the National Science Foundation (NSF; Grant No. OIA-2229498), University of Alabama at Birmingham (UAB) internal startup funds, and a UAB Faculty Development Grant Program, Office of the Provost. L.B. is supported by the DOE-BES (Award No. DE-SC0002613). The National High Magnetic Field Laboratory acknowledges support from the NSF (Cooperative Agreement Grant No. DMR-1644779) and the state of Florida. T.N. acknowledges support from the Swiss National Science Foundation through a consolidator grant (Grant No. TMC2-213805). Z.M. and W.Z. acknowledge support from the National Natural Science Foundation of China (Grant No. 62150410438), the Beihang Hefei Innovation Research Institute (Project No. BHXX-19-02) for growth and beamline 13U of the National Synchrotron Radiation Laboratory for the ARPES experiments. Work at Nanyang Technological University was supported by the National Research Foundation, Singapore, under its Fellowship Award (NRF-NRF13-2021-0010), the Agency for Science, Technology and Research (A*STAR) under its Manufacturing, Trade and Connectivity (MTC) Individual Research Grant (IRG) (Grant No. M23M6c0100), and the Nanyang Assistant Professorship grant (NTU-SUG).

Author contributions M.S.H. conceived the project. The STM experiments were performed by M.S.H. and Y.X.J. in consultation with M.Z.H. F.S. performed the tight-binding calculations. R.I. performed the first-principles calculations. The crystals were grown by Z.M. and W.Z. The ARPES measurements were performed by Z.J.C. and Z.M. The Landau-level calculations were performed by T.H. and M.Y. under the supervision of G.C. The quasiparticle interference calculations were carried out by H.C. under the supervision of G.C. M.S.H., F.S., R.I., T.N., L.B. and M.Z.H. developed the figures and wrote the paper. M.Z.H. supervised the project. All authors discussed the results and participated in the making the interpretation and drawing the conclusion.

Competing interests The authors declare no competing interests.

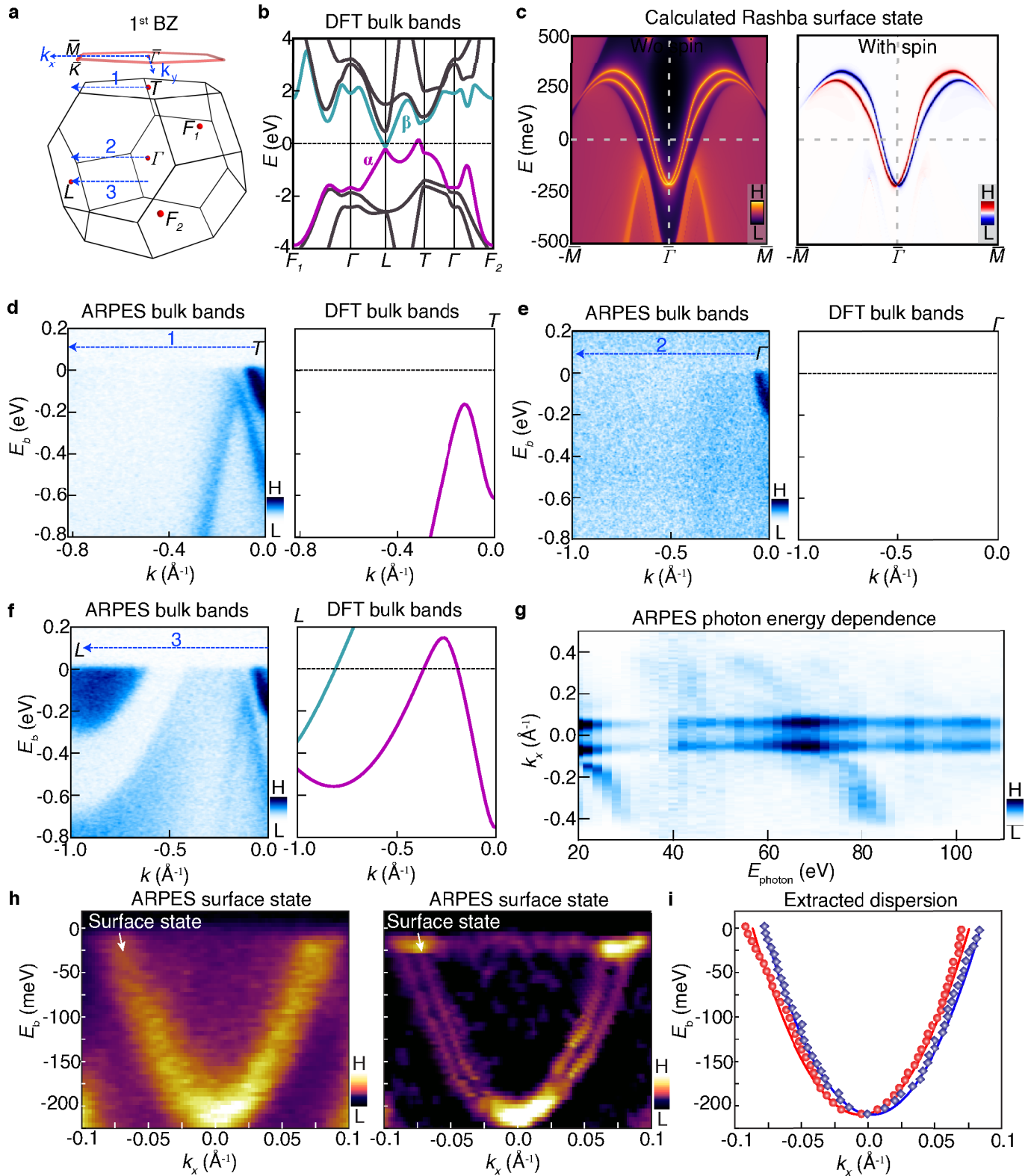
Additional information

Supplementary information The online version contains supplementary material available at <https://doi.org/10.1038/s41586-024-07203-8>.

Correspondence and requests for materials should be addressed to Md Shafayat Hossain, Frank Schindler or M. Zahid Hasan.

Peer review information Nature thanks Enrico Rossi and the other, anonymous, reviewer(s) for their contribution to the peer review of this work. Peer reviewer reports are available.

Reprints and permissions information is available at <http://www.nature.com/reprints>.



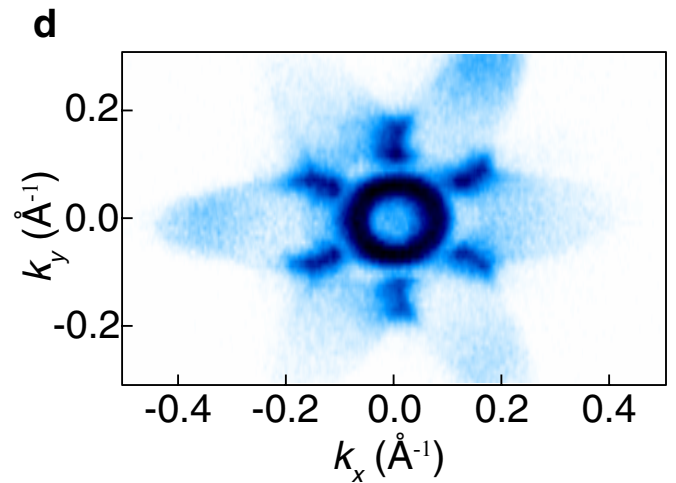
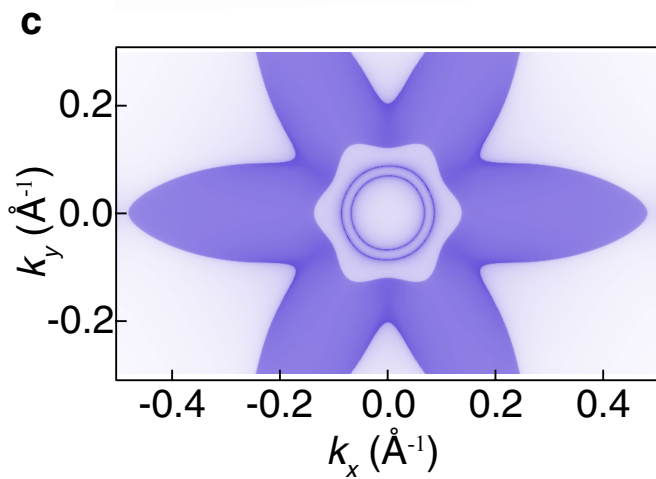
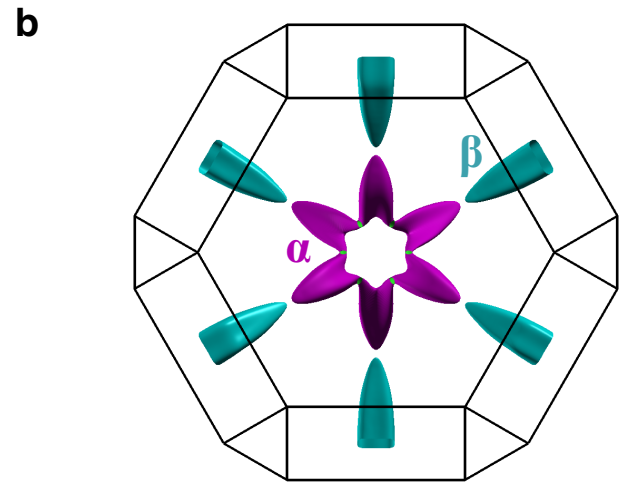
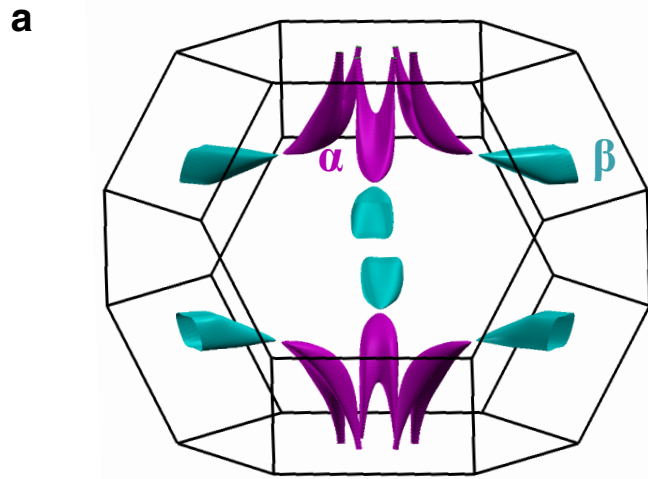
Extended Data Fig. 1 | See next page for caption.

Article

Extended Data Fig. 1 | First-principles calculations and angle-resolved photoemission spectroscopy determination of the electronic band structures.

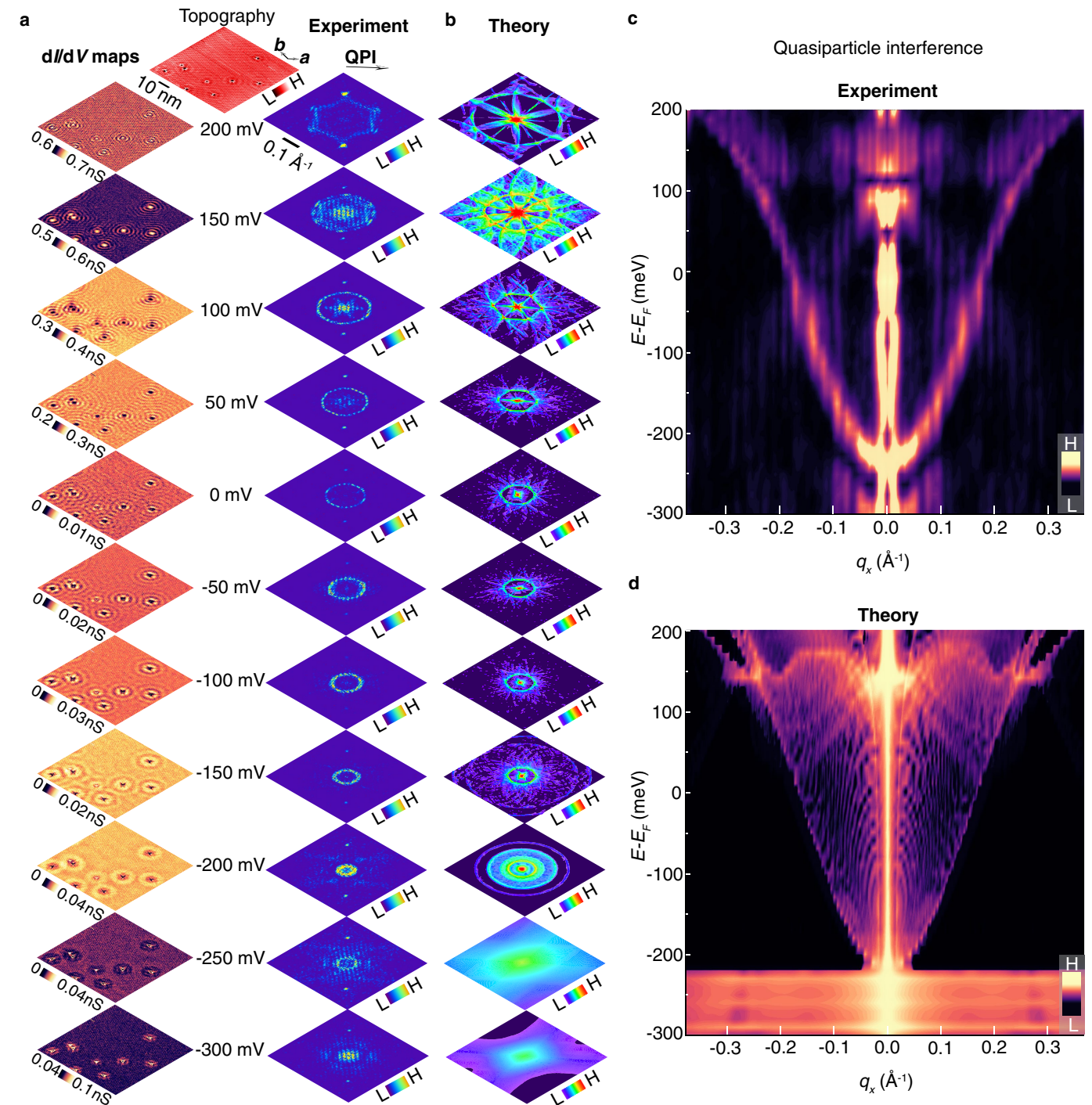
a, First Brillouin zone and the projected surface along (111). Note that L is part of a group of three inequivalent L -points that are related by C_3 rotation symmetry around the z -axis. In the caption of Fig. 4 and the Supplementary Information, these are referred to as L , L' , and L'' . **b**, Electronic band structure of bulk α -As calculated using density functional theory over the whole bulk Brillouin zone, taking into consideration the presence of spin-orbit coupling. The bands crossing the Fermi energy are highlighted in magenta (valence band) and cyan (conduction band). **c**, Left: Calculated surface bands connecting the conduction and valence bands with Rashba-like features. These bands, depicted using bright orange curves, are projected on the (111) surface (also shown in Fig. 1g). Right: Calculated spin texture of the Rashba-like surface bands. **d-f**, Angle-resolved photoemission spectroscopy energy-momentum cuts encompassing high symmetry points \bar{T} (panel **d**), $\bar{\Gamma}$ (panel **e**), and L_3 (panel **f**) of the bulk Brillouin zone. The directions are marked in panel **a** with dashed blue lines. The cuts are measured with a linear-horizontal polarized

light with the photon energies of 67 eV (panel **d**), 40 eV (panel **e**), and 97 eV (panel **f**), respectively. The right panels in **d-f** show the corresponding band structures obtained via first-principles calculations. The bulk bands obtained from photoemission spectroscopy qualitatively match the first-principles results. **g**, Constant energy contour of the photon energy dependence measurement at the Fermi energy. The size of the electron pocket near $\bar{\Gamma}$ does not depend on the photon energy, which confirms its surface-state nature. **h**, Energy-momentum cut (left) and its second derivative (right) taken along $\bar{\Gamma} - \bar{M}$ direction of the surface Brillouin zone, obtained from photoemission spectroscopy on the cleaved (111) surface (ab plane). The spectra were acquired using 22 eV, linear-horizontally polarized light. The topological surface state is marked by the white arrow. The small Rashba splitting is visualized in the second derivative plot (also shown in Fig. 1f). **i**, Extracted dispersion of the Rashba-split surface states, shown using red and blue points. Red and blue curves denote parabolic fits to the photoemission data. These photoemission spectroscopy results are consistent with the first-principles calculations presented in panel **c**.



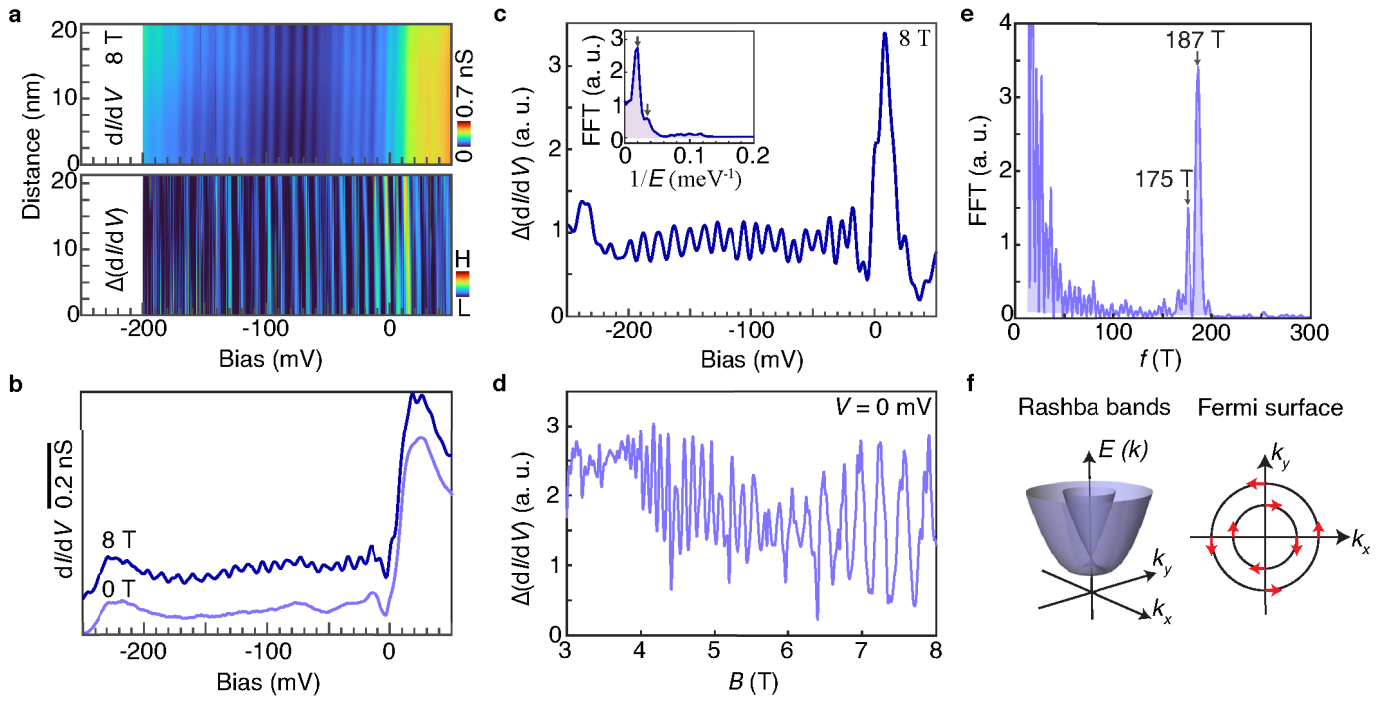
Extended Data Fig. 2 | Fermi surface of α -As obtained via first-principles calculations and photoemission spectroscopy. **a** and **b**, Three-dimensional Fermi surface of α -As featuring a hole-like (α) pocket shown in magenta and an electron-like (β) pocket shown in cyan, originating from the magenta and cyan bands in Extended Data Fig. 1b, respectively. **c**, Fermi surface projected on the (111) surface obtained using first-principles tight-binding calculations. It exhibits

two additional Fermi pockets centered at $k = 0$, due to the Rashba-like surface states. **d**, Fermi surface map taken on the As(111) surface. The map is obtained using 20 eV photon energy and with linear-horizontally polarized light. Photoemission data also show ring-shaped Fermi pockets centering at $k = 0$ in addition to the three-dimensional bulk state.



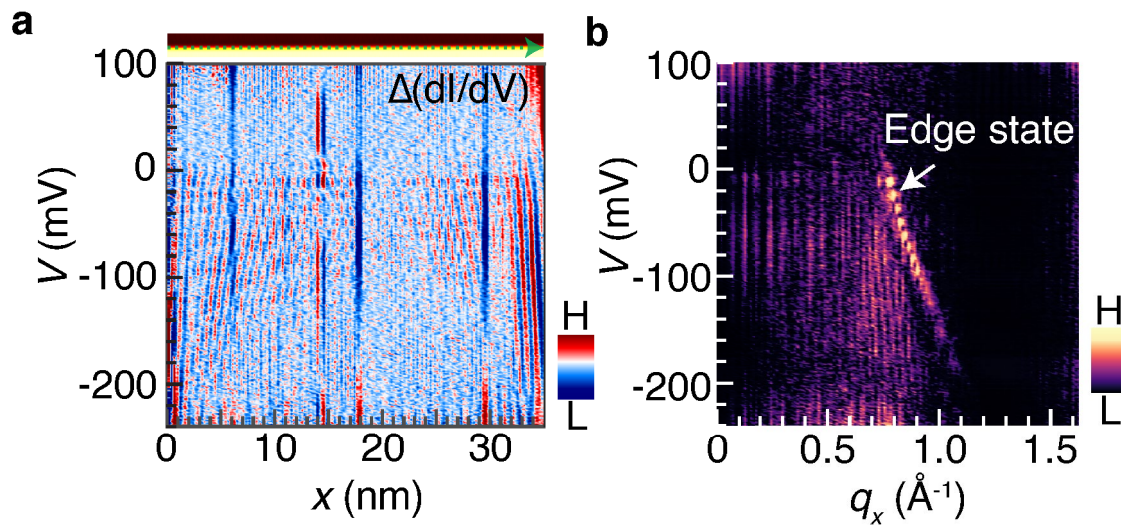
Extended Data Fig. 3 | Quasiparticle interference signature of the surface state. **a**, Large-scale spectroscopic maps (left) and the corresponding Fourier transform at different tip-sample biases; the respective topography is also shown. Clear quasiparticle interference patterns are seen at all the bias voltages. **b**, Calculated quasiparticle interference patterns. The joint density of states method, which takes into account all possible scattering vectors, has been employed for the calculation. **c**, Experimental quasiparticle interference spectrum (energy resolution ≈ 25 meV which is determined by the number of bias points in the tunneling spectrum at each spatial point; q resolution = 0.0015 \AA^{-1} which comes from the dimensions of the scanned area) taken along a high-symmetry direction, marked with an arrow in panel **a**, right column. The spectrum

demonstrates several interference branches. The parabolic-shaped branch, which is the most prominent scattering branch in the quasiparticle interference spectrum, originates from $\sim -230 \pm 15$ meV. This energy position matches the location of the surface band bottom in the photoemission spectroscopy (Fig. 1f) and the first-principles calculation results (Fig. 1g). (A quantitative comparison between the three sets of data is provided in Supplementary Table 1). Therefore, it is most likely that this quasiparticle interference branch stems from the surface state. Tunneling junction set-up for dI/dV maps: $V_{\text{set}} = 200$ mV, $I_{\text{set}} = 1$ nA, $V_{\text{mod}} = 5$ mV. **d**, Calculated quasiparticle interference spectrum, showing a clear parabolic-shaped scattering branch, which is in excellent agreement with the experimental result presented in panel **c**.



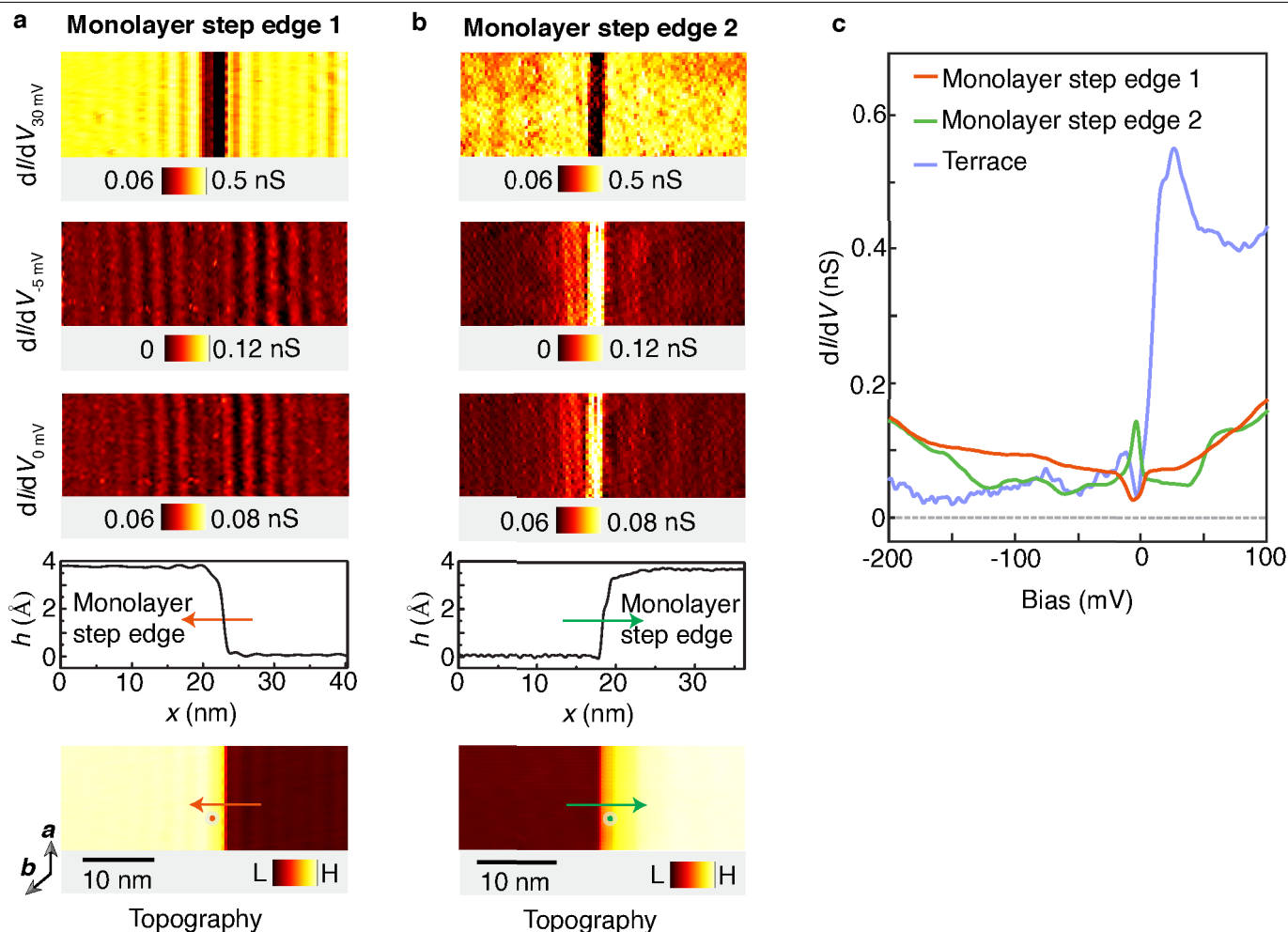
Extended Data Fig. 4 | Landau level spectroscopy of α -As. **a**, dI/dV line map (top) and its derivative (bottom) under $B = 8$ T applied perpendicularly to the cleaved surface. The intense modulation in differential conductance is due to Landau quantization. **b**, Averaged dI/dV spectra at $B = 0$ T, and 8 T taken from the same region clarifying that the dI/dV modulation is due to Landau quantization. **c**, Derivative (to remove the slowly varying background) of the 8 T data and its Fourier transform (inset) showing two (close-by) peaks, suggesting two sets of Landau fans. **d**, Field-dependent differential conductance data obtained from a line cut of the Landau fan (shown in Fig. 1h) at the Fermi energy. **e**, Fourier transform of panel **d** data (after replotting the data as a function of $\frac{1}{\nu}$). Fourier transform magnitude as a function of cyclotron frequency reveals two well-developed peaks at 175 T and 187 T. The two peaks correspond

to the Fermi surface areas (in units of cyclotron frequency) of the two Fermi pockets stemming from the Rashba-split surface state. **f**, Schematic illustration of the Fermi surface stemming from the Rashba bands (see Extended Data Fig. 1c for numerically computed bands). Left: Schematic energy-momentum plot of the parabolic Rashba bands. A cut at the Fermi energy yields two concentric, ring-shaped Fermi pockets. Right: Schematic Fermi surface plot containing the two concentric ring-shaped pockets (see Extended Data Fig. 2c for numerically computed Fermi surfaces). The experimentally obtained 175 T and 187 T peaks (panel **e**) represent the area of the inner and outer ring-shaped Fermi pockets, respectively. Tunneling junction set-up: $V_{\text{set}} = 50$ mV, $I_{\text{set}} = 0.5$ nA, $V_{\text{mod}} = 0.5$ mV.



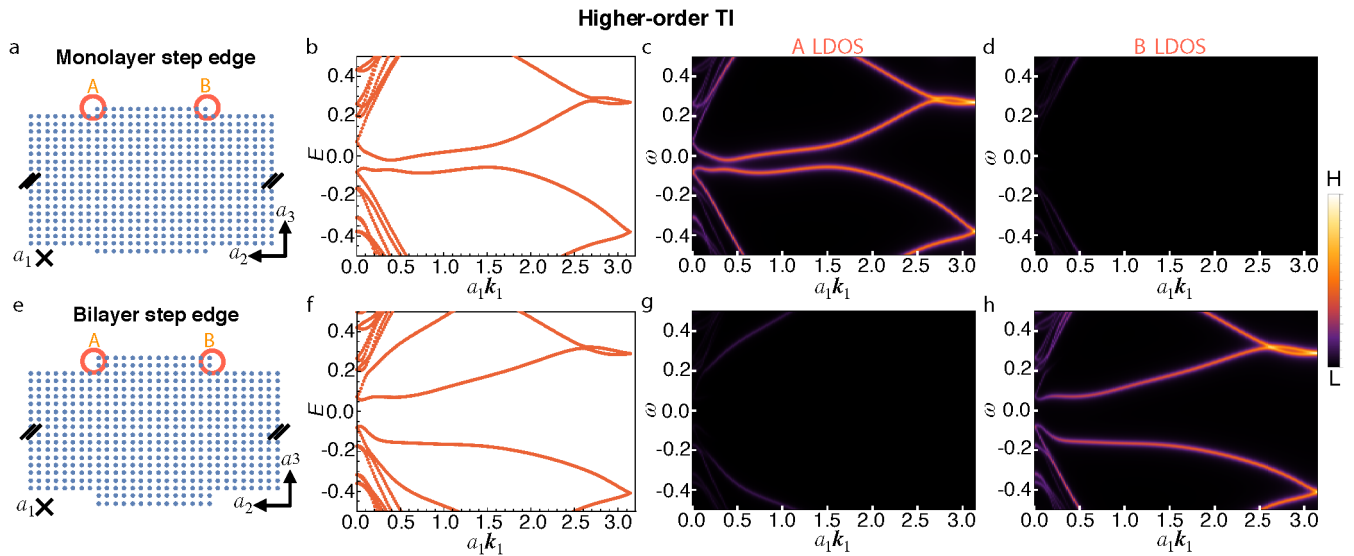
Extended Data Fig. 5 | Line spectroscopy with high spatial and energy resolutions and the corresponding Fourier transform taken along a bilayer step edge. This bilayer step edge, whose orientation is identical to that of the step edges displayed in Fig. 3a and d, manifests a step edge state. **a**, Intensity plot revealing pronounced quantum interference patterns. The green dotted

line on the topographic image (shown at the top) indicates the location where the dI/dV line spectroscopy is performed. The direction of the scan is marked by an arrow. **b**, Corresponding one-dimensional Fourier transform, highlighting a clear edge state dispersion. Tunneling junction set-up: $V_{\text{set}} = 100$ mV, $I_{\text{set}} = 0.5$ nA, $V_{\text{mod}} = 0.5$ mV.



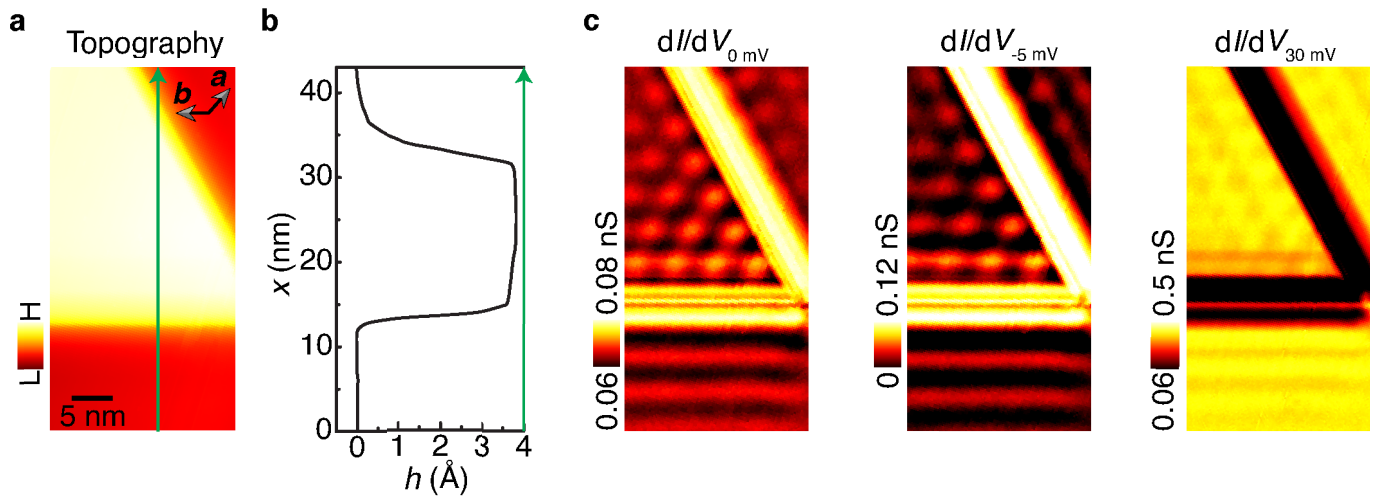
Extended Data Fig. 6 | Orientation-dependence of the monolayer step edge states. **a, b**, Topographic images, height profiles, and the corresponding differential conductance maps around two monolayer step edges (1 and 2 as marked). The color-coded arrows in the topographies and the height profiles indicate the directions from the bottom to the top terraces. Depending on this direction, one monolayer step edge (monolayer step edge 2) exhibits a step edge state while the other monolayer step edge (monolayer step edge 1) does not. **c**, Differential spectra, taken at the monolayer step edge 1 (orange), monolayer step edge 2 (green), and away from the step edges (violet), revealing striking differences between the two step edges. Orange and green dots in the topographic images in panels **a** and **b** denote the respective positions on the monolayer step edges 1 and 2 where the differential spectra are taken. While the

monolayer step edge 2 exhibits a pronounced step edge state, the monolayer step edge 1 features a largely suppressed differential conductance within the soft gap. Note that the monolayer step edge 2 has the same orientation as the monolayer step edge in Fig. 2a, and thereby both exhibit the same electronic structure. On the other hand, resembling the two bilayer step edges shown in Fig. 3a,b, the two monolayer step edges also show a dramatic contrast—one step edge exhibits a pronounced step edge state while the other step edge along the same crystallographic axis, but with a different orientation, does not. Here, however, the orientation favoring a step edge state is opposite to that of the bilayer case (Fig. 3a,b). Tunneling junction set-up for the differential spectra: $V_{\text{set}} = 100$ mV, $I_{\text{set}} = 0.5$ nA, $V_{\text{mod}} = 0.5$ mV. Tunneling junction set-up for dI/dV maps: $V_{\text{set}} = 100$ mV, $I_{\text{set}} = 0.5$ nA, $V_{\text{mod}} = 1$ mV.



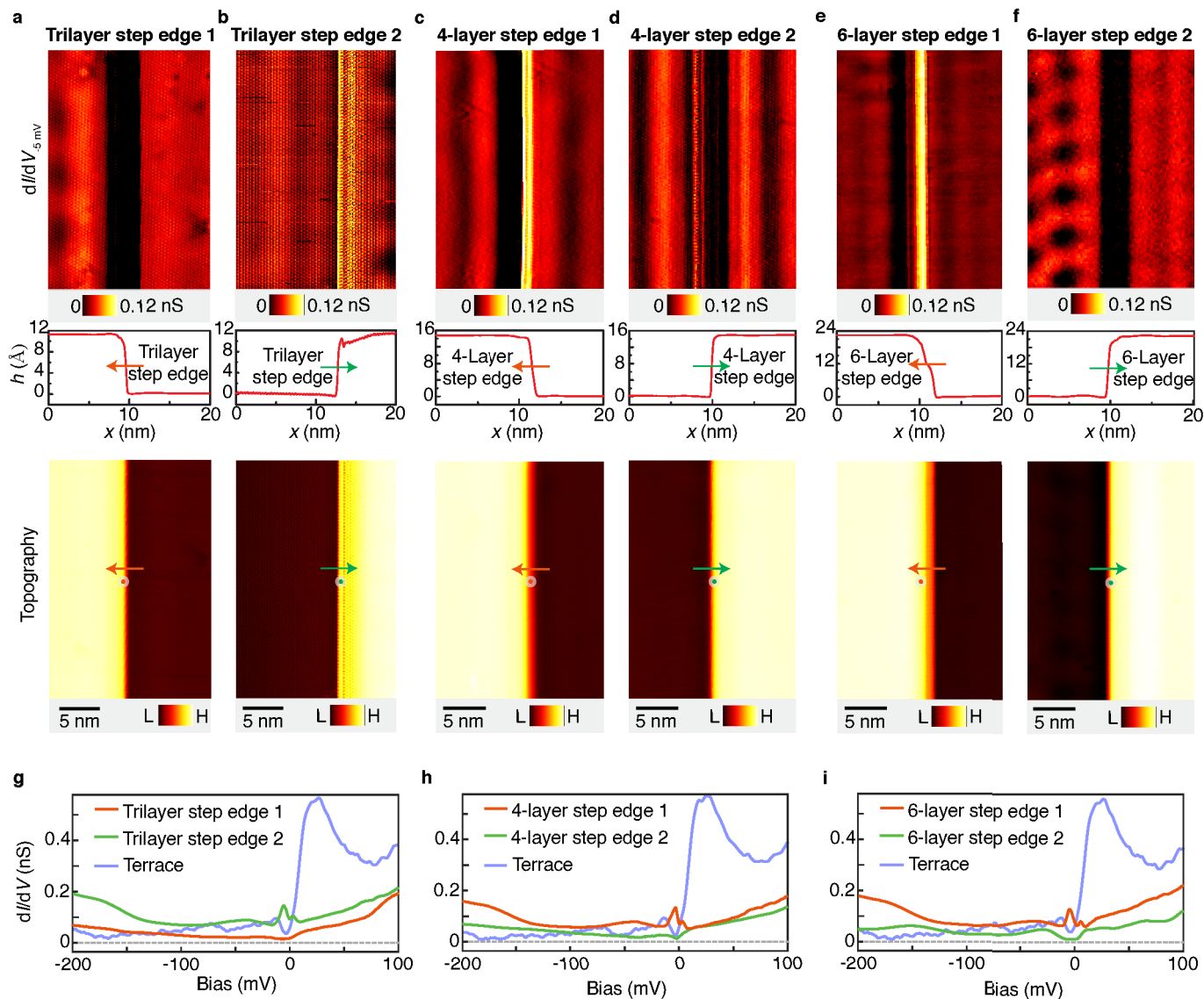
Extended Data Fig. 7 | Low-energy spectra of the tight binding model in absence of first-order topology. Here we delineate the step edge dispersion in a tight-binding system that differs from α -As in that it only has a double band inversion at the Γ point of the bulk Brillouin zone, and not an extra single band inversion at each of the three L, L', L'' points as is the case for α -As. Correspondingly, the model only has nontrivial higher-order topology, but no first-order topology. As derived in our Supplementary Information, such a situation implies a gapped step edge dispersion, however, the gapped modes are precursors of hinge modes localized near the step edges. This situation is schematically depicted in Fig. 4c. **a**, Monolayer step edge geometry. We preserve periodic boundary conditions in the a_1 -direction (the out-of-plane direction, with lattice spacing a_1), so that k_1 is a conserved crystal momentum. There are two step edges, one of type A and one of type B (see Supplementary Information), on each of the top and bottom surfaces. This is the minimal configuration of step edges that preserves inversion symmetry as well as

periodic boundary conditions along the a_2 -direction. **b**, Monolayer step edge dispersion with k_1 using the lattice shown in panel **a**. We only show the momentum range $k_1 \in [0, \pi]$ because the spectrum in the range $k_1 \in [\pi, 2\pi]$ is related by time-reversal symmetry. There is no nontrivial spectral flow (the spectrum is gapped). **c**, Local density of states (LDOS) for the A step edge. The LDOS is large for the low-energy bands closest to the gap, implying that they are well-localized at the step edge. **d**, Local density of states for the B step edge. This LDOS is small, implying that there are no low-energy states at the step edge. **e**, Bilayer step edge geometry. **f**, Bilayer step edge dispersion. There is still a gap, but the low-energy bands are slightly different from the monolayer case. **g**, Local density of states for the A step edge. The LDOS is again large for the low-energy bands, implying that they are well-localized at the same step edge as for the monolayer. **h**, Local density of states for the B step edge. Like the monolayer case, there are no step edge states close to the Fermi level.



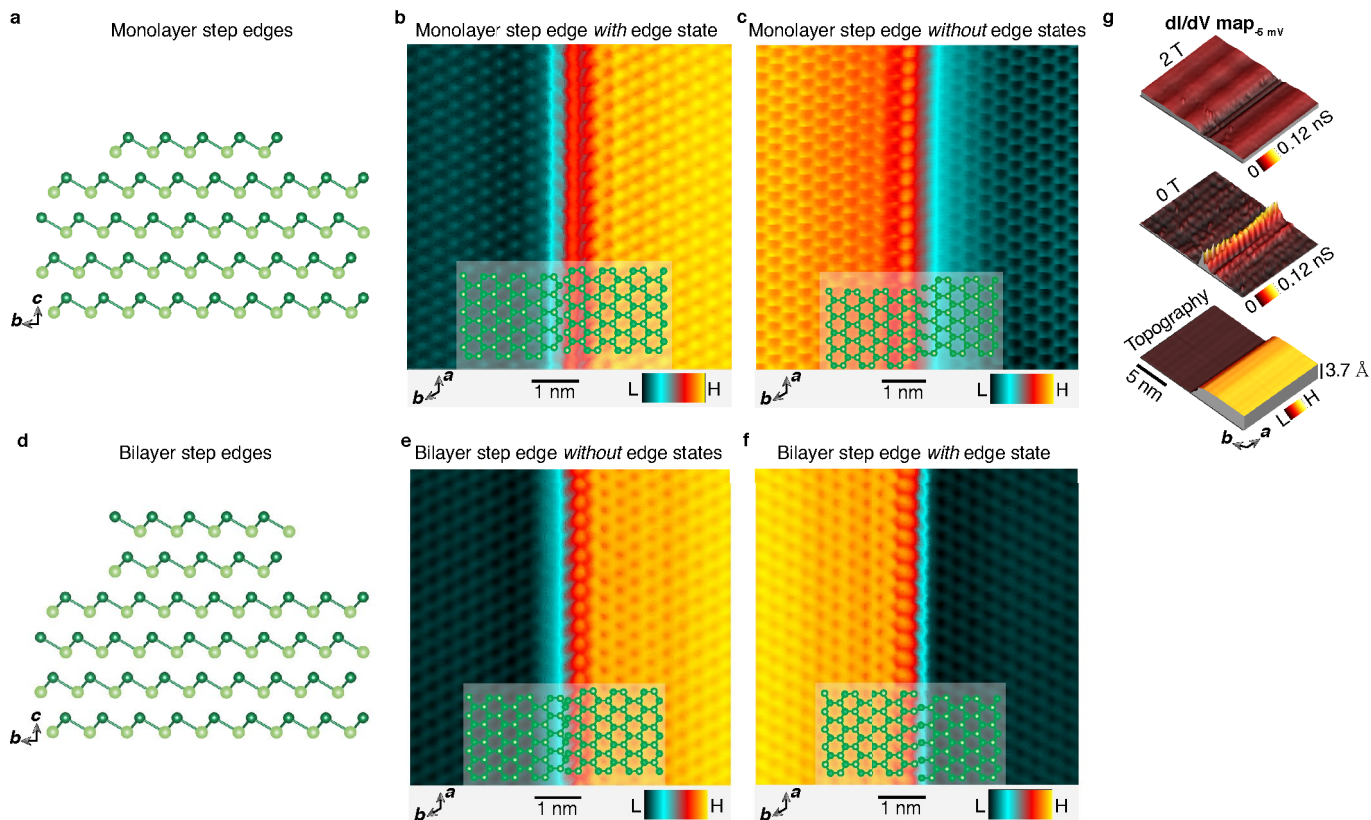
Extended Data Fig. 8 | Step edge states at the monolayer step edges along the b -axis and rotated by 120° with respect to it. **a**, Topographic image of two monolayer step edges along the b -axis and rotated by 120° with respect to it. The orientation of the two step edges is opposite to those of the two monolayer step edges in Fig. 3d. Here the crystal side lies between the two step edges contrary to Fig. 3d, where the crystal side extends away from the pit. **b**, Height profile taken perpendicular to the b -axis direction. The corresponding location is marked on the topographic image in panel **a** with a green line; the direction of the scan is marked with an arrow. **c**, Differential conductance maps at different bias voltages, taken in the region shown in panel **a**. The two monolayer step

edges, along the b -axis and rotated by 120° with respect to it, harbor step edge states that are manifested via an enhanced differential conductance. This behavior is in stark contrast to the monolayer step edges along the same directions, but with opposite orientations (Fig. 3d). Such an orientation dependence is consistent with our other data on different step edges along different crystallographic directions and with different orientations and layer thicknesses. Tunneling junction set-up for the differential spectra: $V_{\text{set}} = 100$ mV, $I_{\text{set}} = 0.5$ nA, $V_{\text{mod}} = 0.5$ mV. Tunneling junction set-up for dI/dV maps: $V_{\text{set}} = 100$ mV, $I_{\text{set}} = 0.5$ nA, $V_{\text{mod}} = 1$ mV.



Extended Data Fig. 9 | Orientation-dependence of the three-, four-, and six-layer-thick step edge states. Topographic images, height profiles, and the corresponding differential conductance maps at $V = -5$ mV around two tri-layer (a and b), four-layer (c and d), and six-layer (e and f) step edges. The color-coded arrows in the topographies and the height profiles indicate the directions from the bottom to the top terraces. Depending on this direction and the layer thickness, certain step edge orientations (such as tri-layer step edge 2, four-layer step edge 1, and six-layer step edge 1) exhibit step edge states, while other orientations (like tri-layer step edge 1, four-layer step edge 2, and six-layer step edge 2) do not. **g-i**, Differential spectra, taken at the two tri-layer (panel g), four-layer (panel h), and six-layer (panel i) step edges, revealing striking differences between the two step edge orientations. Consistent with the orientation dependence of the monolayer step edges in Extended Data Fig. 6, and opposite to that of the bilayer step edges in Fig. 3a,b, the tri-layer step edge 2 (green curve in panel g; dI/dV map in panel b) shows a pronounced step edge

state, while the tri-layer step edge 1 (orange curve in panel g; dI/dV map in panel a) exhibits largely suppressed differential conductance within the soft gap of the surface. Interestingly, this orientation dependence switches for the four-layer step edge, where the four-layer step edge 2 (green curve in panel h; dI/dV map in panel d) lacks a step edge state, while the four-layer step edge 1 (orange curve in panel h; dI/dV map in panel c) carries a strong step edge state. This observation is consistent with the even-odd effect observed between the step edge preferred orientations in mono and bilayer step edges. The six-layer step edge displays a similar geometry dependence as the four-layer step edge, with the six-layer step edge 2 (green curve in panel i; dI/dV map in panel f) lacking a step edge state, while the six-layer step edge 1 (orange curve in panel i; dI/dV map in panel e) exhibits a pronounced step edge state. Tunneling junction set-up for the differential spectra: $V_{\text{set}} = 100$ mV, $I_{\text{set}} = 0.5$ nA, $V_{\text{mod}} = 0.5$ mV. Tunneling junction set-up for dI/dV maps: $V_{\text{set}} = 100$ mV, $I_{\text{set}} = 0.5$ nA, $V_{\text{mod}} = 1$ mV.



Extended Data Fig. 10 | Atomic structure for two different geometric orientations of the mono and bilayer step edges, highlighting the asymmetry between them. **a**, Side view (along the bc plane) of the two monolayer step edges. **b** and **c**, Atomically resolved topographic images of the corresponding monolayer step edges along the a -direction. **d**, Side view (along the bc plane) of the two bilayer step edges. **e** and **f**, Atomically resolved topographic images ($V_{\text{gap}} = 100$ mV, $I_t = 3$ nA) of the corresponding bilayer step edges along the a direction. Notably, there is an asymmetry between the two orientations in both monolayer and bilayer step edges, with one orientation featuring a sharper step edge. Interestingly, this preferred orientation alternates between the mono and bilayer cases, in accordance with the even-odd effect observed in the

step edge states, where the step edge state appears to favor the smoother edge. We note that visualizing atoms directly at the step edge poses challenges due to the abrupt change in height at that location and the small inter-atomic distance (≈ 3.7 Å) in α -As. As a result, the atom arrays at the step edge may not be as clearly visualized in our scanning tunneling microscopy compared to those located away from the step edge. **g**, **Extended scanning tunneling microscopy data:** Topography (bottom) and the corresponding dI/dV maps ($V = -5$ mV) acquired at $B = 0$ T and 2 T. At $B = 2$ T, the spectral weight at the step edge is suppressed. Such a suppression highlights the impact of time-reversal symmetry breaking on the step edge state. Tunneling junction set-up: $V_{\text{set}} = 100$ mV, $I_{\text{set}} = 0.5$ nA, $V_{\text{mod}} = 1$ mV.